

Ultrafast Electron-Lattice Coupling Dynamics in VO₂ and V₂O₃ Thin Films

Elsa Abreu,^{1,2,*} Stephanie N. Gilbert Corder,^{1,3} Sun Jin Yun,^{4,5} Siming Wang,^{6,7,8,9} Juan Gabriel Ramírez,¹⁰ Kevin West,^{11,6,7} Jingdi Zhang,^{6,†} Salinporn Kittiwatanakul,¹¹ Ivan K. Schuller,^{6,7,8} Jiwei Lu,¹¹ Stuart A. Wolf,^{11,12} Hyun-Tak Kim,^{4,5} Mengkun Liu,^{3,‡} and Richard D. Averitt^{6,§}

¹*Both authors contributed equally to this work.*

²*Institute for Quantum Electronics, Department of Physics,
ETH Zurich, 8093 Zurich, Switzerland*

³*Department of Physics and Astronomy,
Stony Brook University, New York, 11794*

⁴*Metal-Insulator Transition Lab, ETRI, Daejeon 305-350, South Korea*

⁵*School of Advanced Device Technology,
University of Science and Technology, Daejeon 305-333, South Korea*

⁶*Department of Physics, The University of California
at San Diego, La Jolla, California 92093, USA*

⁷*Center for Advanced Nanoscience,
The University of California at San Diego, La Jolla, California 92093, USA*

⁸*Materials Science and Engineering Program,
The University of California at San Diego, La Jolla, California 92093, USA*

⁹*Materials Sciences Division, Lawrence Berkeley
National Laboratory, Berkeley, California 94720, USA*

¹⁰*Department of Physics, Universidad de los Andes, Bogotá 111711, Colombia*

¹¹*Department of Materials Science and Engineering,
University of Virginia, Charlottesville VA 22904, USA*

¹²*Department of Physics, University of Virginia, Charlottesville VA 22904, USA*

(Dated: January 20, 2017; Received)

Abstract

Ultrafast optical pump - optical probe and optical pump - terahertz probe spectroscopy were performed on vanadium dioxide (VO_2) and vanadium sesquioxide (V_2O_3) thin films over a wide temperature range. A comparison of the experimental data from these two different techniques and two different vanadium oxides, in particular a comparison of the electronic oscillations generated by the photoinduced longitudinal acoustic modulation, reveals the strong electron-phonon coupling that exists in the metallic state of both materials. The low energy Drude response of V_2O_3 appears more susceptible than VO_2 to ultrafast strain control. Additionally, our results provide a measurement of the temperature dependence of the sound velocity in both systems, revealing a four- to fivefold increase in VO_2 and a three- to fivefold increase in V_2O_3 across the phase transition. Our data also confirm observations of strong damping and phonon anharmonicity in the metallic phase of VO_2 , and suggest that a similar phenomenon might be at play in the metallic phase of V_2O_3 . More generally, our simple table-top approach provides relevant and detailed information about dynamical lattice properties of vanadium oxides, opening the way to similar studies in other complex materials.

I. INTRODUCTION

Vanadium oxides are well known examples of materials where the phases are determined by strong interactions between different degrees of freedom. Such complex systems, where charge, lattice, orbital, and spin contributions can be equally strong and are frequently coupled, exhibit a variety of phenomena including high temperature superconductivity¹, colossal magnetoresistance², multiferroicity³, and topological surface states⁴. Given the complex nature of these materials, the various phases are generally challenging to investigate experimentally. Ultrafast time resolved techniques are a successful route to approach these problems^{5,6}. In particular, time resolved measurements in different energy ranges have contributed to the understanding of insulator-to-metal transitions (IMTs) in vanadium dioxide (VO_2) and vanadium sesquioxide (V_2O_3) as a function of temperature, pressure, or doping⁷⁻¹⁴. These measurements have also shed light onto the nature of the different insulator phases in both systems^{8,15-17}, and the electron-phonon coupling driven acoustic response in V_2O_3 ^{8,9}.

Despite many ultrafast and static measurements, the exact mechanisms responsible for the IMTs in vanadium oxides and especially in VO_2 remain widely debated¹⁸⁻²⁶, namely the contribution of electronic correlations (Mott-Hubbard picture) and of electron-lattice mediated effects (Peierls model)^{16,22,27-29}. It is clear, however, that multiple pathways are possible to initiate pressure and temperature dependent transitions, and that electronic and lattice effects are strongly coupled^{16,17,27,30}. Measurements that dynamically investigate this coupling are therefore essential to assist in understanding the nature of IMTs.

Bulk VO_2 undergoes an IMT at 340 K, along with a monoclinic-to-rutile structural transition^{18,31} (cf. phase diagram in Fig. S1a³²). In the low temperature phase, the vanadium ions dimerize and tilt to form a nonmagnetic insulator²². Above-bandgap photoexcitation of the monoclinic insulator can promote electrons to anti-bonding states, causing repulsion between the dimerized vanadium ions and lattice expansion, followed by long-range shear rearrangements at the speed of sound^{17,21}. Above a critical fluence threshold the metallic phase forms via nucleation and growth^{16,29,33,34}. The acoustic and optical phonon landscape changes drastically across the IMT, and phonons have recently been seen to account for 2/3 of the entropy increase at the IMT and to stabilize the metallic phase^{25,27}. These observations suggest that lattice effects play a significant role in driving the IMT in

VO₂.

V₂O₃ is a low temperature monoclinic antiferromagnetic insulator which transitions to a paramagnetic rhombohedral metal above 155 K^{18,35} (cf. phase diagram in Fig. S1b³²). Initial reports stated that the system exhibits a classical Mott-Hubbard transition where electrons localize to form the insulating phase^{19,20}. However, more recent work points to electron-lattice effects contributing strongly to the first order IMT in the undoped compound^{23,27}, and questions the equivalence of temperature and pressure routes in driving the phase transition in doped V₂O₃¹⁰. The strong strain-dependence of metallic V₂O₃ manifests via the large influence of ultrafast acoustic modulations on the spectral weight redistribution dynamics, particularly in the far infrared region of the spectra corresponding to the low energy Drude weight⁹.

In this work, we present a comparative ultrafast pump-probe study of photoinduced acoustic effects in VO₂ and V₂O₃, present in both optical reflectivity and terahertz (THz) conductivity dynamics. Transient reflectivity measurements at 1.55 eV are sensitive to inter-band transitions in VO₂ and V₂O₃, with insulating gaps of 0.6 eV and 0.5 eV, respectively²², while THz probes the quasiparticle dynamics, effectively yielding a dynamical measurement of the dc conductivity.

Our results show that, similar to V₂O₃^{8,9}, VO₂ exhibits a modulation of the electronic response due to photoinduced acoustic effects. This influence of small structural variations on the electronic behavior attests to significant electron-phonon coupling. Comparing both materials, we observe that V₂O₃ is significantly more amenable than VO₂ to Drude weight modulation via acoustic wave propagation. Also, thin film samples with varying defect density exhibit different static and dynamic electronic responses. Thin films with fewer defects have properties closer to bulk and are therefore characterized by a larger THz conductivity in the metallic state and by larger photoinduced conductivity variations. In contrast to this electronic behavior, the acoustic signatures we observe appear to be quite robust against varying defect density in the thin films. Differences in the response to photoinduced acoustic excitation between VO₂ and V₂O₃, and between nominally equivalent samples, could be related to the strong and distinct influence of defects on the electronic response of these materials³⁰.

In addition, our data provide a temperature dependent measure of the sound velocity in both VO₂ and V₂O₃, revealing an increase in the sound velocity across the insulator-to-metal

transition, four- to fivefold for VO₂ and three- to fivefold for V₂O₃.

We also verify that acoustic damping increases in the metallic phase of VO₂, compared to the insulating phase, in agreement with previous reports that present phonon entropy as a stabilization mechanism for the metallic phase²⁷. V₂O₃ exhibits a similarly increased damping in the metallic phase, hinting that phonon anharmonicity might also be much stronger than in the insulating phase, and that phonon effects might play a significant role in the IMT of this material as well.

II. EXPERIMENTAL METHODS

Transient optical reflectivity measurements were performed using 35 fs pulses at 800 nm (1.55 eV) from a 1 KHz repetition rate, 3 W average power Ti:sapphire regenerative amplifier. Pump and probe fluences were set at 1-4 mJ/cm² and < 10 μJ/cm², respectively, and both beams were set at approximately normal incidence to the sample. THz pulses 1 ps in duration were generated via optical rectification and detected by electro-optic sampling in ZnTe. In contrast to the optical measurements at 1.55 eV, the THz pulses (0.1 - 2.5 THz) effectively probe the low energy Drude response²². Transient optical reflectivity measurements at 800 nm, yielding ΔR/R, and THz conductivity measurements, yielding Δσ⁵, were performed with the same pump conditions.

Of particular relevance to this work is the ability to generate coherent acoustic phonons using ultrafast optical excitation. The ultrafast above bandgap optical pulse is absorbed near the surface causing a localized temperature increase. Thermal expansion leads to a transient stress which launches a strain wave in the material. The propagating acoustic phonon modifies the refractive index and can therefore be detected optically via modulation of ΔR/R, at 800 nm, and of Δσ, around 1 THz. When the film thickness is on the order of the longitudinal acoustic phonon wavelength an acoustic standing wave is generated and detected instead³⁶. Analytical^{37,38} and conceptual³⁶ aspects of the generation and detection of coherent acoustic modulations can be found in the literature³⁶⁻³⁸.

The samples consist of 75 nm and 50 nm thick films of VO₂ on c-cut Al₂O₃³⁹, 75 nm thick films of V₂O₃ on c-cut Al₂O₃⁴⁰, and 95 nm thick films of V₂O₃ on r-cut Al₂O₃³⁰. The VO₂ films have a well defined out of plane rutile c-axis, and three preferred in-plane orientations due to the hexagonal symmetry of the c-cut Al₂O₃ substrate⁴¹. The 75 nm V₂O₃ film has a

well-defined rhombohedral out of plane [110] axis but is polycrystalline in plane, while the 95 nm film is nearly single crystalline throughout. Details of the fabrication can be found elsewhere^{30,39,40}. Unless otherwise specified, the results presented in this paper correspond to the 75 nm films.

The sample temperature was set using a continuous flow cryostat, pumped down to 10^{-6} mbar and equipped with a heating stage.

III. RESULTS

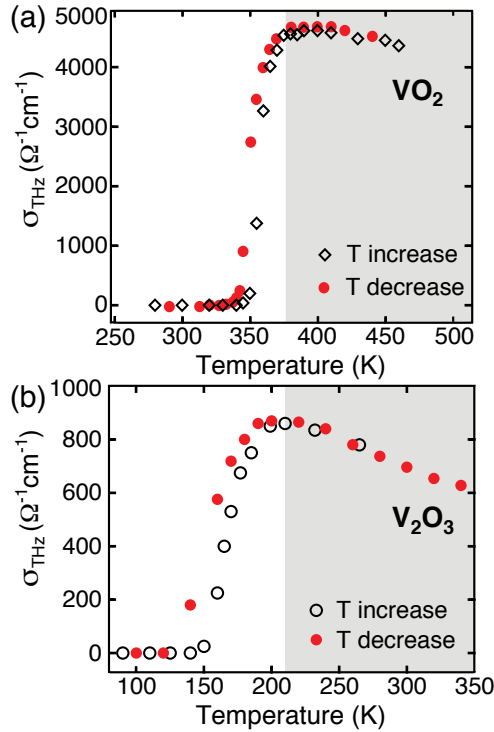


FIG. 1. Temperature dependence of the static far-infrared conductivity for the 75 nm thick (a) VO_2 and (b) V_2O_3 thin films. Open black (solid red) symbols indicate increasing (decreasing) temperature. Both samples display hysteresis, characteristic of first order phase transitions happening at 360 K in VO_2 and at 160 K in V_2O_3 . The fully metallic region is shaded gray.

Figure 1 shows the static THz conductivity of the 75 nm VO_2 and V_2O_3 films measured using THz spectroscopy. Fig. 1a shows that the IMT in the VO_2 film occurs at $T_{IMT} = 360$ K, and that a maximum conductivity of $4800 (\Omega\text{cm})^{-1}$ is obtained at 380 K. V_2O_3 is seen

from Fig. 1b to have $T_{IMT} = 160$ K, with a peak conductivity of $900 (\Omega\text{cm})^{-1}$ at 200 K. These measurements demonstrate that our VO_2 and V_2O_3 films behave similarly to bulk single crystals, which attests to the generality of our conclusions. Above 200 K the V_2O_3 metallic state conductivity decreases dramatically (Fig. S1³²), beyond what would be expected from an increased electron-phonon scattering rate, due to the strongly correlated nature in this “bad” metal region^{22,42}. The relative conductivity decrease in the VO_2 metallic state above 380 K is smaller compared to V_2O_3 , with a 6% conductivity drop per 50 K for VO_2 and an 11 % conductivity drop per 50 K for V_2O_3 . This is consistent with suggestions that electronic correlations have a smaller impact on the metallic phase of VO_2 compared to metallic V_2O_3 ^{43,44}, which enters a crossover region to a pure Mott insulator phase above 450 K (Fig. S1³²). Corresponding temperature-dependent static conductivity data for the 95 nm V_2O_3 film are shown in Fig. S2³².

Figures 2a, 3a and 3b show the transient conductivity ($\Delta\sigma$) and transient reflectivity at 800 nm ($\Delta R/R$) of VO_2 at low (Fig. 2a) and high (Figs. 3a and 3b) initial temperatures for a pump fluence of 3.8 mJ/cm^2 . From the conductivity dynamics at $T < T_{IMT}$, shown in Fig. 2a, it is clear that the maximum value achieved for the transient conductivity $\Delta\sigma(t)$ increases with initial temperature. For $T = 77$ K, $\Delta\sigma(t)$ recovers in less than 10 ps, whereas for $T > 160$ K the deposited energy is sufficient to thermally stabilize the metallic phase beyond our 350 ps measurement window³². As previously observed, the tens of ps timescale for the conductivity increase is considerably larger than the <1 ps electron-phonon thermalization time (Fig. S9³²) due to the nucleation and growth process that accompanies the IMT^{33,45}.

For $T > T_{IMT}$ the metallic phase dominates the transient photothermal response of VO_2 . $\Delta\sigma$, shown in Fig. 3a, decreases following photoexcitation in agreement with Fig. 1a, and so does $\Delta R/R$ (Fig. 3b). Most significantly, the high temperature dynamics of both $\Delta\sigma$ and $\Delta R/R$ exhibit oscillatory components (clearly isolated below, in Figs. 4a and 5b) which are direct signatures of acoustic wave propagation, similar to those reported in V_2O_3 ^{8,9}. Budai *et al.*²⁷ have observed that strongly anharmonic phonons rather than electronic effects stabilize the metallic phase of VO_2 . The results shown here confirm the strength of electron-phonon coupling in metallic VO_2 since acoustic signatures are seen not only in $\Delta R/R$, as expected, but also in $\Delta\sigma$, a clear indication that lattice dynamics modulate the Drude response of the system above T_{IMT} .

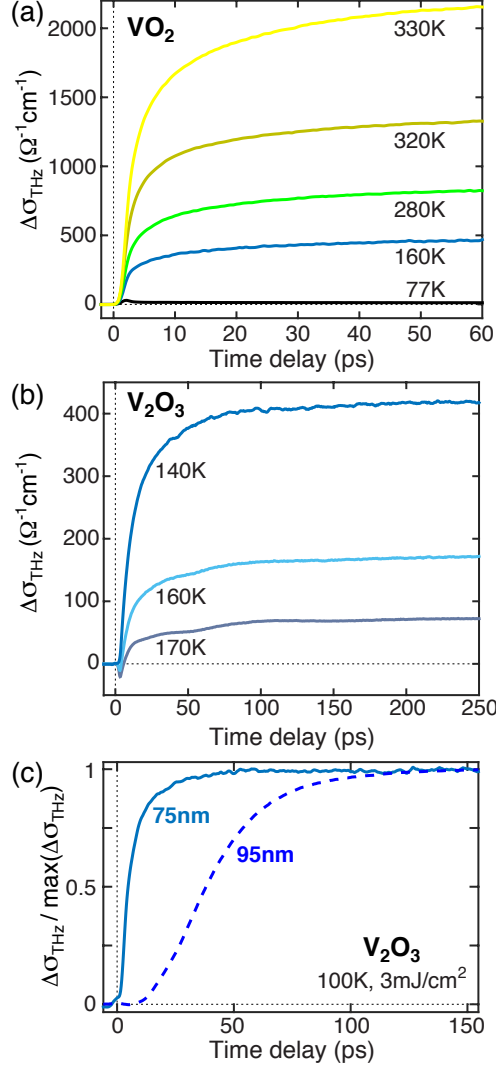


FIG. 2. Transient $\Delta\sigma$ of 75 nm thick VO_2 (a), 75nm thick V_2O_3 (b), and 75 nm and 95 nm thick V_2O_3 (c) for temperatures below T_{IMT} at a pump fluence of 3.8 mJ/cm^2 (a), 1 mJ/cm^2 (b) and 3 mJ/cm^2 (c). Starting in the insulating phase, the THz response consists in a transient conductivity increase which corresponds to the IMT. (c) compares the normalized $\Delta\sigma(t)$ for the 95 nm and 75 nm V_2O_3 films at 100 K, revealing a significant difference in IMT dynamics at short time delays which arises from different defect densities in the films.

As a counterpart to the data on VO_2 , Figs. 2b, 3c and 3d show $\Delta\sigma$ and $\Delta R/R$ for V_2O_3 at temperatures below (Fig. 2b) and above (Figs. 3c and 3d) T_{IMT} for a pump fluence of 1 mJ/cm^2 . V_2O_3 also exhibits a tens of ps $\Delta\sigma$ increase characteristic of a percolative IMT (Fig. 2b). The decrease in $\Delta\sigma$ with increasing initial temperature stems solely from the

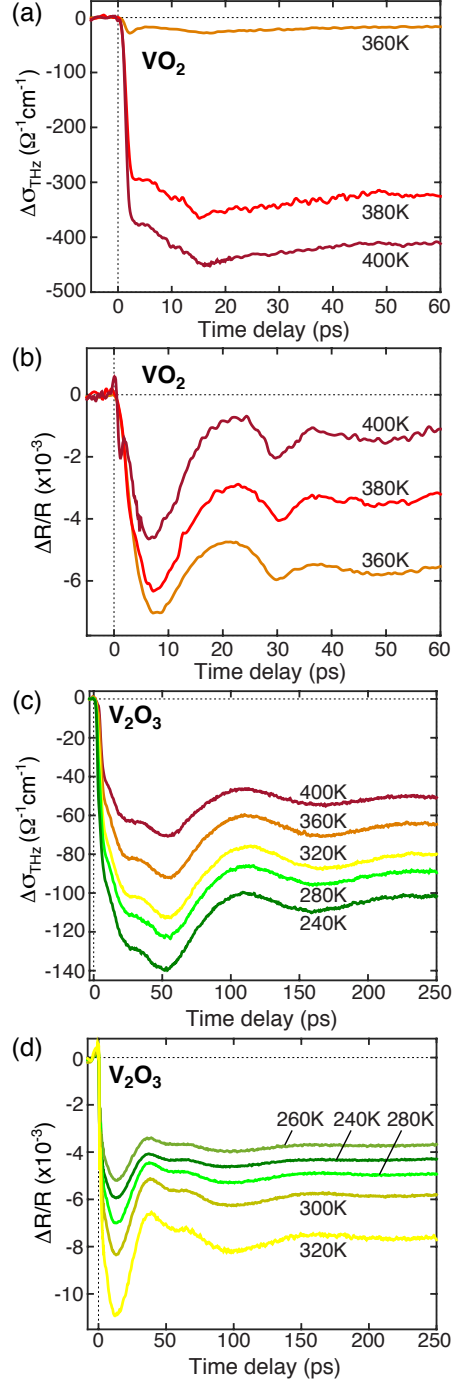


FIG. 3. Transient $\Delta\sigma$ (a, c) and $\Delta R/R$ (b, d) of 75 nm thick VO_2 (a, b) and V_2O_3 (c, d) for temperatures above T_{IMT} at a pump fluence of 3.8 mJ/cm^2 (a, b) and 1 mJ/cm^2 (c, d). Shown are the metallic reflectivity responses, dominated by acoustic signatures, and the metallic conductivity responses, also with clear acoustic signatures.

fact that temperatures closer to T_{IMT} are used compared to VO_2 , so that the initial state already has a finite conductivity (Fig. 1) and the $\Delta\sigma$ response saturates as the full metallic state is reached. Photoexcitation of the system in the metallic phase at $T > T_{IMT}$ produces a decrease of both $\Delta\sigma$ and $\Delta R/R$ in addition to clearly defined temperature dependent acoustic signatures, as previously reported^{8,9}.

Figure 2c compares the normalized $\Delta\sigma(t)$ for the 95 nm and 75 nm V_2O_3 films at 100 K for a pump fluence of 3 mJ/cm². The 95 nm film has a metallic conductivity more than twice as large as the 75 nm film (Fig. 1b and Fig. S2³²), which is likely due to its single crystalline rather than polycrystalline nature and to its consequent smaller defect density. As discussed in an earlier publication⁴⁵, the defect density has a strong influence not only on the static properties but also on the transition dynamics of V_2O_3 thin films since it affects the nucleation and growth of metallic domains in the insulating phase. For V_2O_3 and VO_2 , it is important to distinguish between ultrafast transition dynamics that occur at the microscopic level, independent of the nucleation and growth process, and those that occur at the mesoscopic level where the response is dominated by nucleation and growth. Microscopic effects have been extensively discussed, particularly in the case of VO_2 ^{22,46–48}. Using a THz probe, which is sensitive to the mesoscale dynamics, we observe fast $\Delta\sigma(t)$ transients that start during photoexcitation by the pump pulse for the 75 nm film, whereas the 95 nm film exhibits slower variations and a delayed onset relative to the pump arrival time (Fig. 2c). These significant differences in conductivity dynamics cannot be explained by the minimal difference in film thickness. Rather, they occur due to the 95 nm film containing fewer defects than the 75 nm film, and hence fewer defect-induced preferential nucleation sites, which slows down the photoinduced IMT in the thicker sample⁴⁵. Such mesoscopic effects occur independently in addition to any microscopic modifications, and their effect on the dynamics must be taken into account in studies of both V_2O_3 and VO_2 .

Despite differences in IMT timescales (Figs. 2c and S6³²), high temperature dynamic data for the 50 nm VO_2 film and the 95 nm V_2O_3 film are comparable to the 75 nm films of each material and consequently are shown in Figs. S4 and S7 of the Supplemental Material³².

Finally, $\Delta R/R$ dynamics for VO_2 and V_2O_3 at $T < T_{IMT}$ also exhibit acoustic oscillations characteristic of the insulating phase. The full dynamic insulating responses have many contributing factors and are therefore less straightforward to analyze than the metallic response. As the present work focuses on the acoustic component, the full low temperature

$\Delta R/R$ signals are shown in Fig. S3³². The acoustic signatures of the insulating phase can, however, be compared with the metallic phase results of Figs. 3b and 3d, as shown in Fig. 5 and discussed in Section IV below.

IV. ANALYSIS AND DISCUSSION

In order to analyze the acoustic dynamics in more detail, we subtract all exponential, non-oscillatory contributions to the metallic data in Fig. 3. This procedure is described in the Supplemental Material³², and yields the acoustic contribution to $\Delta\sigma(t)$, shown in Fig. 4, and to the $\Delta R/R$ dynamics, shown in Fig. 5. The lack of acoustic signatures in the insulating phase $\Delta\sigma(t)$ response in Figs. 2a and 2b is expected since the THz probe is only sensitive to the metallic volume fraction⁴⁵.

The acoustic component of the $\Delta\sigma$ dynamics is shown in Fig. 4a and 4b for VO_2 and V_2O_3 , respectively. The modulation is significantly longer lived in V_2O_3 , an indication that phonon damping is smaller in V_2O_3 than in VO_2 . The significance of phonon damping for the properties of VO_2 and V_2O_3 will be discussed in more detail below.

In Fig. 4c, the maximum $\Delta\sigma$ oscillation amplitude for both VO_2 and V_2O_3 is plotted as a function of $T - T_{IMT}$. The maximum is estimated at the time delays marked by vertical gray bars in Figs. 4a and 4b to avoid potential residual contributions from non-acoustic effects at shorter time delays. This choice of temperature scale enables a direct comparison between the different samples and materials. The bottom part of Fig. 4c shows the oscillation amplitude maxima normalized by the static conductivity at that temperature³², while the top shows the non-normalized values. For $T > T_{IMT} + 20$ K, i.e. well outside the hysteresis region (Fig. 1), the absolute value of the maximum conductivity modulation (top of Fig. 4c) decreases with increasing temperature for all films. This decrease is consistent with the negative slope of the static conductivity observed with increasing temperature in the metallic phase (Figs. 1 and S2³²). Interestingly, the conductivity oscillation amplitudes are very similar for all the samples examined, even after accounting for the differences in pump fluence (the fluence dependence for the two V_2O_3 samples is discussed in Section II G and Fig. S8 of the Supplemental Material³²). In particular, oscillation amplitudes are comparable for VO_2 and V_2O_3 , as well as for samples of the same material with different static conductivities. The normalized plot in Fig. 4c (bottom) enables a more direct comparison of VO_2 and V_2O_3

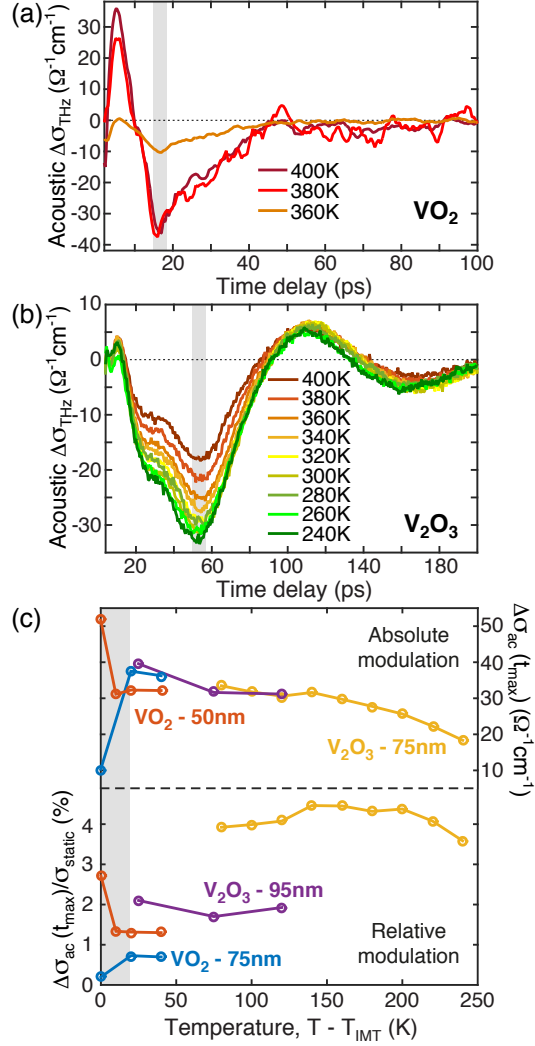


FIG. 4. Background subtracted $\Delta\sigma$ acoustic oscillations for (a) VO₂ and (b) V₂O₃, corresponding to the data from Figs. 3a and 3c. $\Delta\sigma(t)$ data for the VO₂ film were smoothed using a five point (1 ps) moving average. Vertical gray bars indicate the time delays at which the values in (c) were calculated³². (c) Bottom: Temperature dependence of the maximum acoustic modulation of $\Delta\sigma$, normalized by the static conductivity at the corresponding temperature (Figs. 1 and S2³²). Top: Temperature dependence of the absolute maximum acoustic modulation of $\Delta\sigma$. Data is shown for all four VO₂ and V₂O₃ films. A fluence of 3.8 mJ/cm² was used for the 75 nm thick VO₂ film (blue), 4 mJ/cm² for the 50 nm VO₂ (orange), 1 mJ/cm² for the 75 nm V₂O₃ (yellow) and 3 mJ/cm² for the 95 nm V₂O₃ (purple). The gray shaded region corresponds to temperatures $T < T_{\text{IMT}} + 20$ K, where the influence of the IMT hysteresis could affect the results.

results. It is clear that acoustic modulations in the 75 nm thick V_2O_3 are stronger than in VO_2 , which points to larger electron-phonon induced strain modulation. This conclusion is further strengthened if the different pump fluences are taken into account when analyzing the data (cf. Section II G and Fig. S8 of the Supplemental Material³²). The 95 nm thick V_2O_3 film does not show such a strikingly higher effect compared to VO_2 .

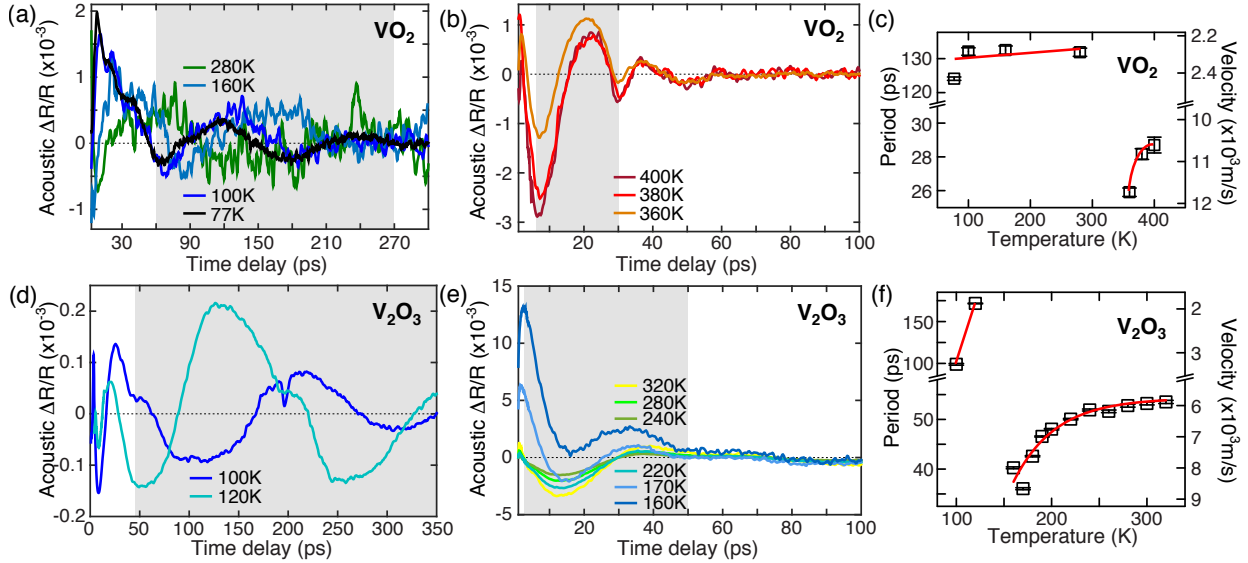


FIG. 5. Background subtracted $\Delta R/R$ acoustic oscillations for insulating (a) and metallic (b) VO_2 and for insulating (d) and metallic (e) V_2O_3 , corresponding to the data in Figs. 3b, 3d and S3³². Plots to the right show the temperature dependence of the acoustic oscillation period and of the corresponding sound velocity for VO_2 (c) and for V_2O_3 (f), calculated by fitting the shaded regions of a, b, d and e with a damped sinusoid. Red lines are linear fits (c, f: insulating phase), an exponential guide to the eye (c: metallic phase) and an exponential fit (f: metallic phase).

It is not trivial to relate the acoustic oscillation period in $\Delta\sigma(t)$ with the sound velocity in the system since the THz probe, with its $\sim 300 \mu\text{m}$ wavelength, effectively probes an average acoustic modulation of the conductivity in the sub-micron thick films⁹. However, an approximate sound velocity value can be directly determined using oscillations of $\Delta R/R$, the transient reflectivity at 800 nm ³⁷.

We focus on the acoustic oscillations which are isolated in Fig. 5, obtained from the data in Figs. 3b and 3d for $T > T_{IMT}$, and in Fig. S3³² for $T < T_{IMT}$. Acoustic modulations of $\Delta R/R$ for $T < T_{IMT}$ are more difficult to observe in V_2O_3 than in VO_2 as the current

measurements are limited to temperatures above 80 K. Indeed, the lower value of T_{IMT} for V_2O_3 compared to VO_2 , as well as the fact that the latent heat is smaller and therefore the IMT can be driven at the same fluence for lower temperatures relative to the respective T_{IMT} , means that the acoustic response of the insulating phase in V_2O_3 is quickly masked by phase transition dynamics. This problem could be circumvented in future work by analyzing the response at lower temperatures or by studying doped V_2O_3 samples.

The period of the reflectivity oscillations shown in Figs. 5c and 5f is determined by fitting the shaded regions in the corresponding reflectivity data with a damped sinusoid. The fidelity of the fit is validated by the near unity adjusted R^2 values (cf. Section II D of the Supplemental Material³²). Given that the 75 nm thickness of the films is on the order of acoustic phonon wavelengths⁴⁹, the observed oscillations are essentially reflections of the acoustic wave that propagates in the sample between the film surface and the film-substrate interface, as described in Section I. The corresponding sound velocity can therefore be calculated from the period, τ , using $v_{sound} = 4d/\tau$ ^{36,37}, where d is the film thickness (a more detailed analysis is given in Section III and Fig. S9 of the Supplemental Material, for a thicker film³²).

The most striking effect in our data is that the sound velocity associated with these oscillations, apart from a slow and monotonic increase with temperature, exhibits an abrupt increase at T_{IMT} when going from the insulating to the metallic phase, by a factor of 4-5 in VO_2 and 3-5 in V_2O_3 . This is seen clearly in Figs. 5c and 5f. Such a large sound velocity variation is not unexpected in vanadium oxides, where lattice constants change by about 1% across the structural phase transition that accompanies the IMT^{32,35,50}. V-O and V-V bond lengths change by up to 4% across the structural transition, stabilizing an insulating phase below T_{IMT} or a metallic phase above T_{IMT} ^{31,32,51}.

Sound velocity measurements for the metallic phase of VO_2 yield approximately 4×10^3 m/s, measured along the rutile c-axis by Maurer *et al.*²⁵, or 8×10^3 m/s, determined from the phonon dispersion of the longitudinal acoustic mode along the Γ -Z direction in Budai *et al.*²⁷. In the metallic phase of V_2O_3 Seikh *et al.*⁴⁹ and Yelon *et al.*⁵² report 8×10^3 m/s, corresponding to longitudinal acoustic mode propagation. The VO_2 and V_2O_3 metallic sound velocities measured in Fig. 5 are consistent with the order of magnitude reported previously. Some discrepancies are expected, as discussed below.

Sample to sample variation in vanadium oxides, and in particular in vanadium oxide

thin films, is well known and must be taken into account when analyzing and comparing different data sets⁵³. In particular, variation in sound velocity values is a result of the different strain environments and crystallinity of the samples. The strain sensitivity of VO₂ material properties, in particular, is widely reported^{53–57} and is caused by large differences in lattice constant values along different crystallographic axes with large variations of these values across the IMT (Table SI³²). For the measurements presented here, the sound velocity determination could be affected by acoustic waves propagating at an angle to the film normal, by substrate-induced strain in the growth direction, as well as by contributions from other acoustic modes in the system, in particular non-longitudinal waves.

Analyzing Figs. 5b and 5e from the perspective of acoustic modulation damping reveals that the amplitude of the metallic oscillations decays two times faster in VO₂ than in V₂O₃ (Fig. 5), with damping times of about 10 ps and 20 ps, respectively³². Damping effects are thus stronger in the metallic phase of VO₂ compared to V₂O₃. The observations from Budai *et. al.*²⁷ of increased phonon damping in the metallic phase compared to the insulating phase are verified by our analysis on VO₂, where the damping time decreases from 145 ps in the insulator to 10 ps in the metal. The results for V₂O₃ show a decrease in damping time from 225 ps in the insulating phase to 20 ps in the metallic phase, suggesting a similar influence of phonon anharmonicity to be at play in the metallic phase of V₂O₃. It should be noted that an additional source of damping exists, due to transmission of the acoustic wave into the substrate. Transmission losses will depend on how well acoustic impedances are matched between the film and the substrate, and can potentially lead to an increase of the effective damping time associated with the VO₂ or V₂O₃ material responses alone. Quantitative comparisons with damping times obtained from other methods must therefore be done with care. A detailed analysis of the observed damping is presented in Section II D of the Supplemental Material³².

Figures 4 and 5 therefore enable us to conclude that acoustic signatures are qualitatively the same and quantitatively within a factor of two of each other in VO₂ and V₂O₃. This is so despite differences in the mechanism that drives the IMT, in particular the larger effect expected from electronic correlations in V₂O₃ compared to VO₂, and in the latent heat associated with the IMT (65 J/cm³ for V₂O₃⁵⁸ and 240 J/cm³ for VO₂⁵⁹). In the remainder of the manuscript we discuss the possible origin of the larger acoustic modulation signal that is observed for V₂O₃. First, the electron-phonon coupling coefficient is higher for V₂O₃

($3 \times 10^{18} \text{ W K}^{-1} \text{ m}^{-3}$)³²) than for VO_2 ($10^{18} \text{ W K}^{-1} \text{ m}^{-3}$)⁶⁰), which partially explains the increased signal strength since energy couples more efficiently between the electrons and the lattice. This means that the strain wave generation process following electronic photoexcitation is more efficient in V_2O_3 , and that the subsequent strain-induced modifications of the electronic spectral weight are stronger. In fact, metallic V_2O_3 at atmospheric conditions is seen to lie near a transition line to a pressure induced isostructural paramagnetic insulating phase (Fig. S1), so that one would indeed expect a similar pressure change to lead to a larger change in the conductivity for V_2O_3 than for VO_2 . Second, the lattice structure of V_2O_3 is overall more amenable to modulations, as deduced from the lower phonon damping measured in V_2O_3 compared to VO_2 which effectively means that the structure is less rigid. This implies that photoinduced strain modulations would be larger in V_2O_3 for the same amount of energy transferred to the lattice. Lastly, it is important to reiterate the strong influence of differences in defect density, which lead to variations in the static and dynamic properties of both VO_2 and V_2O_3 when comparing nominally equivalent samples. In particular, such variations are known to affect the structural response of these materials³⁰, and should therefore be taken into account when attempting precise quantitative comparisons.

V. CONCLUSION

This work demonstrates that strong electron-phonon coupling exists and is responsible for clear ultrafast acoustic modulations of the Drude and optical responses in V_2O_3 and VO_2 . This effect appears to be stronger for V_2O_3 than for VO_2 , suggesting that the electronic and lattice structure of V_2O_3 is more amenable to transient strain modulation than VO_2 .

We further identify a significant temperature dependence of the sound velocity in both materials, in particular a dramatic increase by a factor of about 4-5 in VO_2 and 3-5 in V_2O_3 across the IMT. The observation (in both materials) of stronger acoustic damping in the metallic phase relative to the insulating one confirms the strong role of phonon anharmonicity in metallic VO_2 and suggests that a similar mechanism is at play in V_2O_3 . The timescale for damping of the acoustic modulations in both the THz conductivity (Drude response) and the near infrared reflectivity (spectral weight at 1.55 eV, related to the occupation of V3d orbitals) are longer for V_2O_3 than for VO_2 , indicating stronger damping in the latter and thus a potentially stronger phonon anharmonicity contribution.

Our findings demonstrate that transient strain induced by photoexcitation is a useful tool to both analyze and control the electronic properties of complex materials and their coupling to lattice excitations. The same approach could be used to investigate the modifications to the electronic and lattice properties induced by different defect densities. This is particularly relevant in the case of VO_2 and V_2O_3 , where different defect densities lead to strong sample to sample variation of static and dynamic properties, but is likely applicable to other complex materials and to their properties which are characteristically sensitive to small perturbations.

VI. ACKNOWLEDGEMENTS

We thank Mariano Trigo and Gabriel Lantz for useful discussions.

E. A. acknowledges support from the ETH Zurich Postdoctoral Fellowship Program and from the Marie Curie Actions for People COFUND Program. R. D. A. and E. A. acknowledges support from DOE—Basic Energy Sciences under Grant No. DE-FG02-09ER46643. S. J. Y. and H.-T. K. acknowledge support from the MIT project at ETRI. I. K. S., S. W., J. G. R. and K. W. acknowledge support from AFOSR under Grant No. FA9550-12-1-0381. One of us (I.K.S.) acknowledges support from the Vannevar Bush Faculty Fellowship program sponsored by the Basic Research Office of the Assistant Secretary of Defense for Research and Engineering and funded by the Office of Naval Research through grant N00014-15-1-2848. J. G. R. kindly acknowledges support from FAPA program through Facultad de Ciencias and Vicerrectoria de Investigaciones of Universidad de los Andes, Bogotá, Colombia, and Colciencias No. 120471250659.

* elsabreu@phys.ethz.ch. Previously at Department of Physics, Boston University, Boston MA 02215, USA

† Previously at Department of Physics, Boston University, Boston MA 02215, USA

‡ mengkun.liu@stonybrook.edu. Previously at Department of Physics, Boston University, Boston MA 02215, USA

§ raveritt@physics.ucsd.edu. Previously at Department of Physics, Boston University, Boston MA 02215, USA

¹ M. Hashimoto, E. A. Nowadnick, R.-H. He, I. M. Vishik, B. Moritz, Y. He, K. Tanaka, R. G.

- Moore, D. Lu, Y. Yoshida, M. Ishikado, T. Sasagawa, K. Fujita, S. Ishida, S. Uchida, H. Eisaki, Z. Hussain, T. P. Devereaux, and Z.-X. Shen, *Nature Materials* **14**, 37 (2014).
- ² S. Jin, T. H. Tiefel, M. McCormack, R. A. Fastnacht, R. Ramesh, and L. H. Chen, *Science* **264**, 413 (1994).
- ³ T. Kubacka, J. A. Johnson, M. C. Hoffmann, C. Vicario, S. de Jong, P. Beaud, S. Grübel, S.-W. Huang, L. Huber, L. Patthey, Y.-D. Chuang, J. J. Turner, G. L. Dakovski, W.-S. Lee, M. P. Minitti, W. Schlotter, R. G. Moore, C. P. Hauri, S. M. Koochpayeh, V. Scagnoli, G. Ingold, S. L. Johnson, and U. Staub, *Science* **343**, 1333 (2014).
- ⁴ Y. H. Wang, H. Steinberg, P. Jarillo-Herrero, and N. Gedik, *Science* **342**, 453 (2013).
- ⁵ R. D. Averitt and A. J. Taylor, *Journal of Physics: Condensed Matter* **14**, R1357 (2002).
- ⁶ J. Orenstein, *Physics Today* **65**, 44 (2012).
- ⁷ O. V. Misochko, M. Tani, K. Sakai, K. Kisoda, S. Nakashima, V. N. Andreev, and F. A. Chudnovsky, *Physical Review B* **58**, 12789 (1998).
- ⁸ B. Mansart, D. Boschetto, S. Sauvage, A. Rousse, and M. Marsi, *Europhysics Letters* **92**, 6 (2010).
- ⁹ M. K. Liu, B. Pardo, J. Zhang, M. M. Qazilbash, S. J. Yun, Z. Fei, J. H. Shin, H.-T. Kim, D. N. Basov, and R. D. Averitt, *Physical Review Letters* **107**, 066403 (2011).
- ¹⁰ F. Rodolakis, P. Hansmann, J. P. Rueff, A. Toschi, M. W. Haverkort, G. Sangiovanni, A. Tanaka, T. Saha-Dasgupta, O. K. Andersen, K. Held, M. Sikora, I. Alliot, J. P. Itié, F. Baudelet, P. Wzietek, P. Metcalf, and M. Marsi, *Physical Review Letters* **104**, 047401 (2010).
- ¹¹ A. Cavalleri, C. Tóth, C. W. Siders, J. A. Squier, F. Ráksi, P. Forget, and J. C. Kieffer, *Physical Review Letters* **87**, 237401 (2001).
- ¹² M. A. Huber, M. Plankl, M. Eisele, R. E. Marvel, F. Sandner, T. Korn, C. Schller, J. R. F. Haglund, R. Huber, and T. L. Cocker, *Nano Letters* **16**, 1421 (2016).
- ¹³ B. T. O’Callahan, A. C. Jones, J. Hyung Park, D. H. Cobden, J. M. Atkin, and M. B. Raschke, *Nature Communications* **6**, 6849 (2015).
- ¹⁴ G. Lantz, B. Mansart, D. Grieger, D. Boschetto, N. Nilforoushan, E. Papalazarou, N. Moisan, L. Perfetti, V. L. R. Jacques, D. L. Bolloc’h, C. Laulhé, S. Ravy, J. P. Rueff, T. E. Glover, M. P. Hertlein, Z. Hussain, S. Song, M. Chollet, M. Fabrizio, and M. Marsi, *Nature Communications* **8**, 13917 (2017).
- ¹⁵ A. Pashkin, C. Kübler, H. Ehrke, R. Lopez, A. Halabica, R. F. Haglund, R. Huber, and

- A. Leitenstorfer, *Physical Review B* **83**, 195120 (2011).
- ¹⁶ D. Wegkamp, M. Herzog, L. Xian, M. Gatti, P. Cudazzo, C. L. McGahan, R. E. Marvel, R. F. Haglund, A. Rubio, M. Wolf, and J. Stähler, *Physical Review Letters* **113**, 216401 (2014).
- ¹⁷ A. X. Gray, J. Jeong, N. P. Aetukuri, P. Granitzka, Z. Chen, R. Kukreja, D. Higley, T. Chase, A. H. Reid, H. Ohldag, M. A. Marcus, A. Scholl, A. T. Young, A. Doran, C. A. Jenkins, P. Shafer, E. Arenholz, M. G. Samant, S. S. P. Parkin, and H. A. Dürr, *Physical Review Letters* **116**, 116403 (2016).
- ¹⁸ F. J. Morin, *Physical Review Letters* **3**, 34 (1959).
- ¹⁹ D. B. McWhan, T. Rice, and J. P. Remeika, *Physical Review Letters* **23**, 1384 (1969).
- ²⁰ D. B. McWhan, J. P. Remeika, T. M. Rice, W. F. Brinkman, J. P. Maita, and A. Menth, *Physical Review Letters* **27**, 941 (1971).
- ²¹ P. Baum, D.-S. Yang, and A. H. Zewail, *Science* **318**, 788 (2007).
- ²² M. M. Qazilbash, A. A. Schafgans, K. S. Burch, S. J. Yun, B. G. Chae, B. J. Kim, H.-T. Kim, and D. N. Basov, *Physical Review B* **77**, 115121 (2008).
- ²³ P. Pfalzer, G. Obermeier, M. Klemm, S. Horn, and M. L. DenBoer, *Physical Review B* **73**, 144106 (2006).
- ²⁴ P. Limelette, A. Georges, D. Jérôme, P. Wzietek, P. Metcalf, and J. M. Honig, *Science* **302**, 89 (2003).
- ²⁵ D. Maurer, A. Leue, R. Heichele, and V. Müller, *Physical Review B* **60**, 13249 (1999).
- ²⁶ L. Baldassarre, A. Perucchi, D. Nicoletti, A. Toschi, G. Sangiovanni, K. Held, M. Capone, M. Ortolani, L. Malavasi, M. Marsi, P. Metcalf, P. Postorino, and S. Lupi, *Physical Review B* **77**, 113107 (2008).
- ²⁷ J. D. Budai, J. Hong, M. E. Manley, E. D. Specht, C. W. Li, J. Z. Tischler, D. L. Abernathy, A. H. Said, B. M. Leu, L. A. Boatner, R. J. McQueeney, and O. Delaire, *Nature* **515**, 535 (2014).
- ²⁸ Z. Tao, T.-R. T. Han, S. D. Mahanti, P. M. Duxbury, F. Yuan, C.-Y. Ruan, K. Wang, and J. Wu, *Physical Review Letters* **109**, 166406 (2012).
- ²⁹ V. R. Morrison, R. P. Chatelain, K. L. Tiwari, A. Hendaoui, A. Bruháes, M. Chaker, and B. J. Siwick, *Science* **346**, 445 (2014).
- ³⁰ J. G. Ramírez, T. Saerbeck, S. Wang, J. Trastoy, M. Malnou, J. Lesueur, J.-P. Crocombette, J. E. Villegas, and I. K. Schuller, *Physical Review B* **91**, 205123 (2015).

- ³¹ M. Marezio, D. B. McWhan, J. P. Remeika, and P. D. Dernier, *Physical Review B* **5**, 2541 (1972).
- ³² See Supplemental Material at ?
- ³³ D. J. Hilton, R. P. Prasankumar, S. Fourmaux, A. Cavalleri, D. Brassard, M. A. El Khakani, J. C. Kieffer, A. J. Taylor, and R. D. Averitt, *Physical Review Letters* **99**, 226401 (2007).
- ³⁴ S. Lysenko, V. Vikhnin, A. Rúa, F. Fernández, and H. Liu, *Physical Review B* **82**, 205425 (2010).
- ³⁵ D. B. McWhan and J. P. Remeika, *Physical Review B* **2**, 3734 (1970).
- ³⁶ S. Ge, X. Liu, X. Qiao, Q. Wang, Z. Xu, J. Qiu, P.-H. Tan, J. Zhao, and D. Sun, *Scientific Reports* **4**, 5722 (2014).
- ³⁷ C. Thomsen, J. Strait, Z. Vardeny, H. J. Maris, J. Tauc, and J. J. Hauser, *Physical Review Letters* **53**, 989 (1984).
- ³⁸ C. Thomsen, H. T. Grahn, H. J. Maris, and J. Tauc, *Physical Review B* **34**, 4129 (1986).
- ³⁹ K. G. West, J. Lu, J. Yu, D. Kirkwood, W. Chen, Y. Pei, J. Claassen, and S. A. Wolf, *Journal of Vacuum Science & Technology A* **26**, 133 (2008).
- ⁴⁰ S. J. Yun, J. W. Lim, J. S. Noh, B. J. Kim, and H. T. Kim, *Japanese Journal of Applied Physics* **48**, 04C139 (2009).
- ⁴¹ S. Kittiwatanakul, *Study of metal-insulator transition in strongly correlated vanadium dioxide thin films*, Ph.D. thesis (2014), section 2.3.2.
- ⁴² M. M. Qazilbash, K. S. Burch, D. Whisler, D. Shrekenhamer, B. G. Chae, H.-T. Kim, and D. N. Basov, *Physical Review B* **74**, 205118 (2006).
- ⁴³ D. N. Basov, R. D. Averitt, D. Van Der Marel, M. Dressel, and K. Haule, *Reviews of Modern Physics* **83**, 471 (2011).
- ⁴⁴ M. K. Stewart, D. Brownstead, S. Wang, K. G. West, J. G. Ramírez, M. M. Qazilbash, N. B. Perkins, I. K. Schuller, and D. N. Basov, *Physical Review B* **85**, 205113 (2012).
- ⁴⁵ E. Abreu, S. Wang, J. G. Ramírez, M. Liu, J. Zhang, K. Geng, I. K. Schuller, and R. D. Averitt, *Physical Review B* **92**, 085130 (2015).
- ⁴⁶ D. J. Hilton, R. P. Prasankumar, S. Fourmaux, A. Cavalleri, D. Brassard, M. A. El Khakani, J. C. Kieffer, A. J. Taylor, and R. D. Averitt, *Physical Review Letters* **99**, 226401 (2007).
- ⁴⁷ M. K. Liu, M. Wagner, E. Abreu, S. Kittiwatanakul, A. McLeod, Z. Fei, M. Goldflam, S. Dai, M. M. Fogler, J. Lu, S. A. Wolf, R. D. Averitt, and D. N. Basov, *Physical Review Letters* **111**,

096602 (2013).

- ⁴⁸ S. A. Dönges, O. Khatib, B. T. OCallahan, J. M. Atkin, J. H. Park, D. Cobden, and M. B. Raschke, *Nano Letters* **16**, 3029 (2016).
- ⁴⁹ M. M. Seikh, C. Narayana, A. K. Sood, P. Murugavel, M. W. Kim, P. A. Metcalf, J. M. Honig, and C. N. R. Rao, *Solid State Communications* **138**, 466 (2006).
- ⁵⁰ D. Kucharczyk and T. Niklewski, *Journal of Applied Crystallography* **12**, 370 (1979).
- ⁵¹ P. D. Dernier and M. Marezio, *Physical Review B* **2**, 3771 (1970).
- ⁵² W. B. Yelon and J. E. Keem, *Solid State Communications* **29**, 775 (1979).
- ⁵³ M. Liu, A. J. Sternbach, M. Wagner, T. V. Slusar, T. Kong, S. L. Bud'ko, S. Kittiwatanakul, M. M. Qazilbash, A. McLeod, Z. Fei, E. Abreu, J. Zhang, M. Goldflam, S. Dai, G.-X. Ni, J. Lu, H. A. Bechtel, M. C. Martin, M. B. Raschke, R. D. Averitt, S. A. Wolf, H.-T. Kim, P. C. Canfield, and D. N. Basov, *Physical Review B* **91**, 245155 (2015).
- ⁵⁴ J. B. Goodenough, *Journal of Solid State Chemistry* **3**, 490 (1971).
- ⁵⁵ J. Wu, Q. Gu, B. S. Guiton, N. P. D. Leon, L. Ouyang, and H. Park, *Nano Letters* **6**, 2313 (2006).
- ⁵⁶ J. H. Park, J. M. Coy, T. S. Kasirga, C. Huang, Z. Fei, S. Hunter, and D. H. Cobden, *Nature* **400**, 431 (2013).
- ⁵⁷ S. Kittiwatanakul, S. A. Wolf, and J. Lu, *Applied Physics Letters* **105**, 073112 (2014).
- ⁵⁸ H. Keer, D. Dickerson, H. Kuwamoto, H. Barros, and J. Honig, *Journal of Solid State Chemistry* **19**, 95 (1976).
- ⁵⁹ G. Chandrashekar, H. Barros, and J. Honig, *Materials Research Bulletin* **8**, 369 (1973).
- ⁶⁰ M. Liu, H. Y. Hwang, H. Tao, A. C. Strikwerda, K. Fan, G. R. Keiser, A. J. Sternbach, K. G. West, S. Kittiwatanakul, J. Lu, S. A. Wolf, F. G. Omenetto, X. Zhang, K. A. Nelson, and R. D. Averitt, *Nature* **487**, 345 (2012).

Supplemental Material to Ultrafast Electron-Lattice Coupling Dynamics in VO₂ and V₂O₃ Thin Films

Elsa Abreu,^{1,2,*} Stephanie N. Gilbert Corder,^{1,3} Sun Jin Yun,^{4,5} Siming Wang,^{6,7,8,9} Juan Gabriel Ramírez,¹⁰ Kevin West,^{11,6,7} Jingdi Zhang,^{6,†} Salinporn Kittiwatanakul,¹¹ Ivan K. Schuller,^{6,7,8} Jiwei Lu,¹¹ Stuart A. Wolf,^{11,12} Hyun-Tak Kim,^{4,5} Mengkun Liu,^{3,‡} and Richard D. Averitt^{6,§}

¹*Both authors contributed equally to this work.*

²*Institute for Quantum Electronics, Department of Physics,
ETH Zurich, 8093 Zurich, Switzerland*

³*Department of Physics and Astronomy,
Stony Brook University, New York, 11794*

⁴*Metal-Insulator Transition Lab, ETRI, Daejeon 305-350, South Korea*

⁵*School of Advanced Device Technology,
University of Science and Technology, Daejeon 305-333, South Korea*

⁶*Department of Physics, The University of California
at San Diego, La Jolla, California 92093, USA*

⁷*Center for Advanced Nanoscience,
The University of California at San Diego, La Jolla, California 92093, USA*

⁸*Materials Science and Engineering Program,
The University of California at San Diego, La Jolla, California 92093, USA*

⁹*Materials Sciences Division, Lawrence Berkeley
National Laboratory, Berkeley, California 94720, USA*

¹⁰*Department of Physics, Universidad de los Andes, Bogotá 111711, Colombia*

¹¹*Department of Materials Science and Engineering,
University of Virginia, Charlottesville VA 22904, USA*

¹²*Department of Physics, University of Virginia, Charlottesville VA 22904, USA*

(Dated: January 19, 2017; Received)

I. PHASE DIAGRAMS OF VO₂ AND V₂O₃

Figure S1 shows the phase diagrams of VO₂ (Fig. S1a) and V₂O₃ (Fig. S1b), illustrating the different phases mentioned in the main text¹⁻⁶. The samples studied are undoped and mostly unstrained (except for some minimal interfacial strain from the lattice mismatch with the sapphire substrate, which has a different structure). The effect of heating, triggered by a static temperature increase or via photoexcitation, is indicated by the red dashed line in each diagram. Note in Fig. S1b that as the V₂O₃ sample temperature increases above 200 K the material approaches a crossover region from a correlated paramagnetic metal to a paramagnetic insulator. This is likely related to the decrease in static conductivity observed in Figure 1b of the main text⁷.

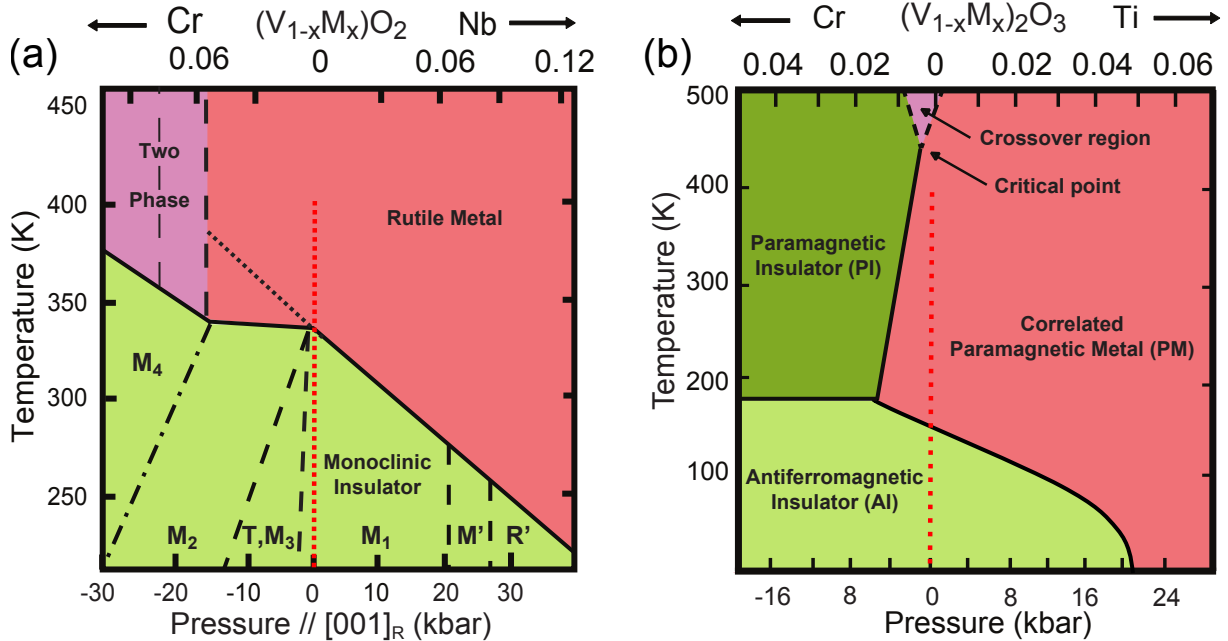


FIG. S1. Phase diagram of single crystalline (a) VO₂ and (b) V₂O₃, adapted from Liu *et al.*³⁻⁶ and Abreu *et al.*^{1,2}. Pressure and chemical doping (M = Cr or Nb for VO₂, and M = Cr or Ti for V₂O₃) are approximately equivalent in both compounds⁸, as indicated by the corresponding x-axes. The samples are undoped and not purposely strained, so that their properties follow the red dashed lines on the phase diagrams.

The temperature induced IMT in unstrained pure VO₂ and pure V₂O₃ is accompanied by a structural phase transition during which lattice parameters change by about 1%^{9,10}. V-O

VO₂		V₂O₃	
Parameter	I → M [%]	Parameter	I → M [%]
Volume	+0.044	Volume	-1.4
a_m (c_R)	-1.0	c_H	+0.2
b_m (a_R)	+0.6	a_H	-0.9
c_m	-0.2	—	—
V-O equatorial	-2.1	—	—
V-O apical	+1.8	—	—
V-O average	-0.8	V-O average	-0.6
V-V average	-3.6	V-V average	-2.8

TABLE SI. Relative variation of the volume, lattice parameters, V-O bond lengths and V-V bond lengths with increasing temperature across the IM and structural phase transitions, for VO₂ (left) and V₂O₃ (right)⁹⁻¹². VO₂ lattice parameters are shown for monoclinic axes (insulating structure), with corresponding rutile axes (metallic structure) where applicable⁹. V₂O₃ lattice parameters are shown for hexagonal axes, which are true hexagonal axes in the rhombohedral metallic phase and pseudo-hexagonal axes in the monoclinic insulating phase¹⁰.

and V-V bond lengths are also modified by 1-20%^{11,12}. Relative changes in these quantities are shown in Table SI, as a reference for the discussion in the main text.

II. COMPLEMENTARY DATA AND DISCUSSION

A. Static Far-infrared Conductivity

Figure S2 shows the temperature dependence of the static conductivity for the 95 nm thick V₂O₃ film. The maximum conductivity of about 1850 Ω⁻¹cm⁻¹ is reached at 210 K, following an IMT at $T_{IMT} = 175$ K. The open black (solid red) symbols show increasing (decreasing) temperature, and the fully metallic region is shaded gray. The single crystallinity and smaller defect density of the 95 nm V₂O₃ film produces a narrower hysteresis, higher transition temperature and larger metallic conductivity than what is reported in Figure 1b for the polycrystalline 75 nm thick V₂O₃ film. The conductivity decrease in the metallic phase is

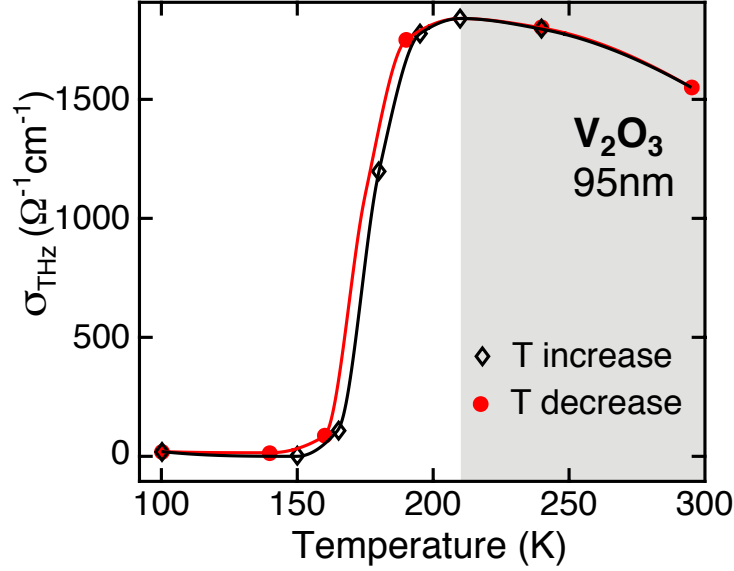


FIG. S2. Temperature dependence of the static far-infrared conductivity for the 95 nm thick V_2O_3 thin film, reproduced from Abreu *et al.*¹³. Open black (solid red) symbols indicate increasing (decreasing) temperature. The sample displays hysteresis, characteristic of the first order phase transition happening at 175 K. The fully metallic region is shaded gray.

comparable between the two samples (10.5 % conductivity drop per 50 K for the 75 nm film vs. 9.2 % conductivity drop per 50 K for the 95 nm film).

Detailed temperature dependent static conductivity measurements are not available for the 50 nm VO_2 film, which is however known to have a broader hysteresis than the 75 nm film. The maximum conductivity and T_{IMT} values used in Fig. 4 of the main text were estimated by comparing the low temperature $\Delta\sigma$ behavior for the 50 nm (Fig. S6b) and 75 nm (Figs. 2a and S6a) films. The maximum $\Delta\sigma$ for the 50 nm film ($1100 \Omega^{-1}\text{cm}^{-1}$) is about half that for the 75 nm ($2400 \Omega^{-1}\text{cm}^{-1}$). Also, $\Delta\sigma$ decreases to $\sim 20\%$ of its maximum value, due to the transition into the metallic phase, at a temperature of about 350 K for the 75 nm film and 330 K for the 50 nm film, i.e. 20 K lower for the latter. By comparing these values to the static data for the 75 nm thick film (Fig. 1a of the main text), a maximum conductivity of $\frac{4800}{2} = 2400 \Omega^{-1}\text{cm}^{-1}$ and a $T_{\text{IMT}} = 360 - 20 = 340$ K can therefore be estimated for the 50 nm film. Given the broader hysteresis of the 50 nm film T_{IMT} could be overestimated by up to 30 K, which would have no significant impact of the conclusions drawn from Fig. 4c of the main text. In general, variations in transition temperatures with

film thickness is not uncommon in vanadates and can have several origins, the most common being slightly different strain environments^{14,15}.

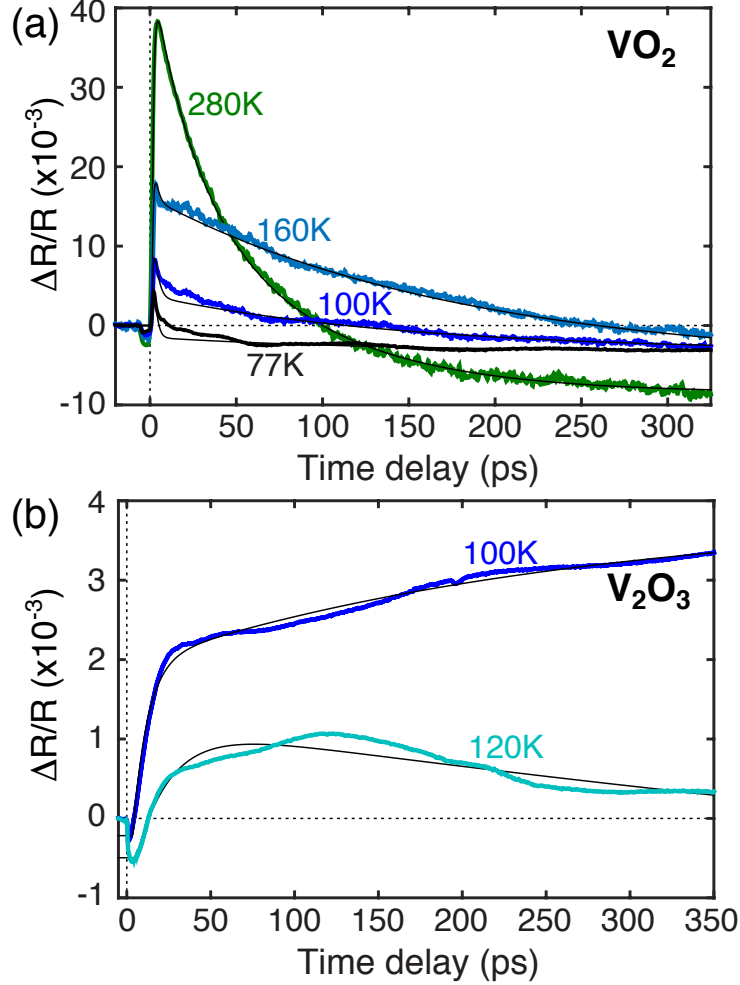


FIG. S3. Transient $\Delta R/R$ in the 75 nm (a) VO_2 and (b) V_2O_3 films for temperatures below T_{IMT} at pump fluences of 3.8 mJ/cm^2 and 1 mJ/cm^2 , respectively. Superimposed onto the data are black lines corresponding to fits to a sum of exponentials, as detailed in the text. The background-subtracted acoustic $\Delta R/R$ oscillations derived from this data are shown in Figs. 5a and 5d of the main text.

B. Low temperature VO_2 and V_2O_3 reflectivity dynamics

The full set of low temperature $\Delta R/R$ data used to extract the acoustic responses shown in Figs. 5a and 5d of the main text is depicted in Fig. S3. The overall optical reflectivity

dynamics are quite complex, especially close to the IMT. An initial sub-picosecond transient in $\Delta R/R$, due to carrier photoexcitation across the insulating bandgap and subsequent electronic thermalization, is observed in both materials. This is followed by a transient response with a characteristic timescale on the picosecond scale, due to equilibration of the electronic temperature with that of the lattice. Subsequent $\Delta R/R$ dynamics track the evolution of the 1.55 eV spectral weight, due essentially to V3d - V3d transitions, as an increasingly large metallic volume fraction is created following photoexcitation (leading to an increasing conductivity, as seen in Fig. S6). The slower dynamics of the metallic phase are the most sensitive to the acoustic modulation effects discussed here.

The exact details of the $\Delta R/R$ dynamics near the IMT goes beyond the scope of this work¹⁶. For the purpose of our analysis, the background dynamics for both materials can be phenomenologically fit by a sum of at most three exponentials. These fits are shown as black lines in Fig. S3. The slow acoustic oscillations are isolated by subtracting this exponentially decaying background from the raw data. The resulting acoustic oscillations are shown in Figs. 5a and 5d of the main text.

C. High temperature VO₂ and V₂O₃ reflectivity and conductivity dynamics

Figure S4 depicts the full time window for the $T > T_{IMT}$ data shown in Figs. 2-5 of the main text, for all four films (50 nm and 75 nm thick VO₂, and 75 nm and 95 nm thick V₂O₃). Figures S4a and S4b show the metallic $\Delta R/R$ and $\Delta\sigma$ transient response for the 75 nm thick VO₂ film, respectively. Figure S4c shows the $\Delta\sigma$ transient response for the 50 nm thick VO₂ film. Figures S4d and S4e show the metallic $\Delta R/R$ and $\Delta\sigma$ transient response for the 75 nm thick V₂O₃ film, respectively. Figure S4f shows the $\Delta\sigma$ transient response for the 95 nm thick V₂O₃ film. The black lines are the fits used to extract the acoustic response as discussed in Section II B.

D. Fitting $\Delta R/R$ with a damped sinusoid, damping timescale

After subtracting the exponential dynamics described above, and shown as black lines in Figs. S3 and S4, one obtains the oscillatory behavior depicted in Figs. 4 and 5 of the main text. For the 75 nm films, the $\Delta R/R$ oscillatory data from Figs. 5a, 5b, 5d and 5e are fit to

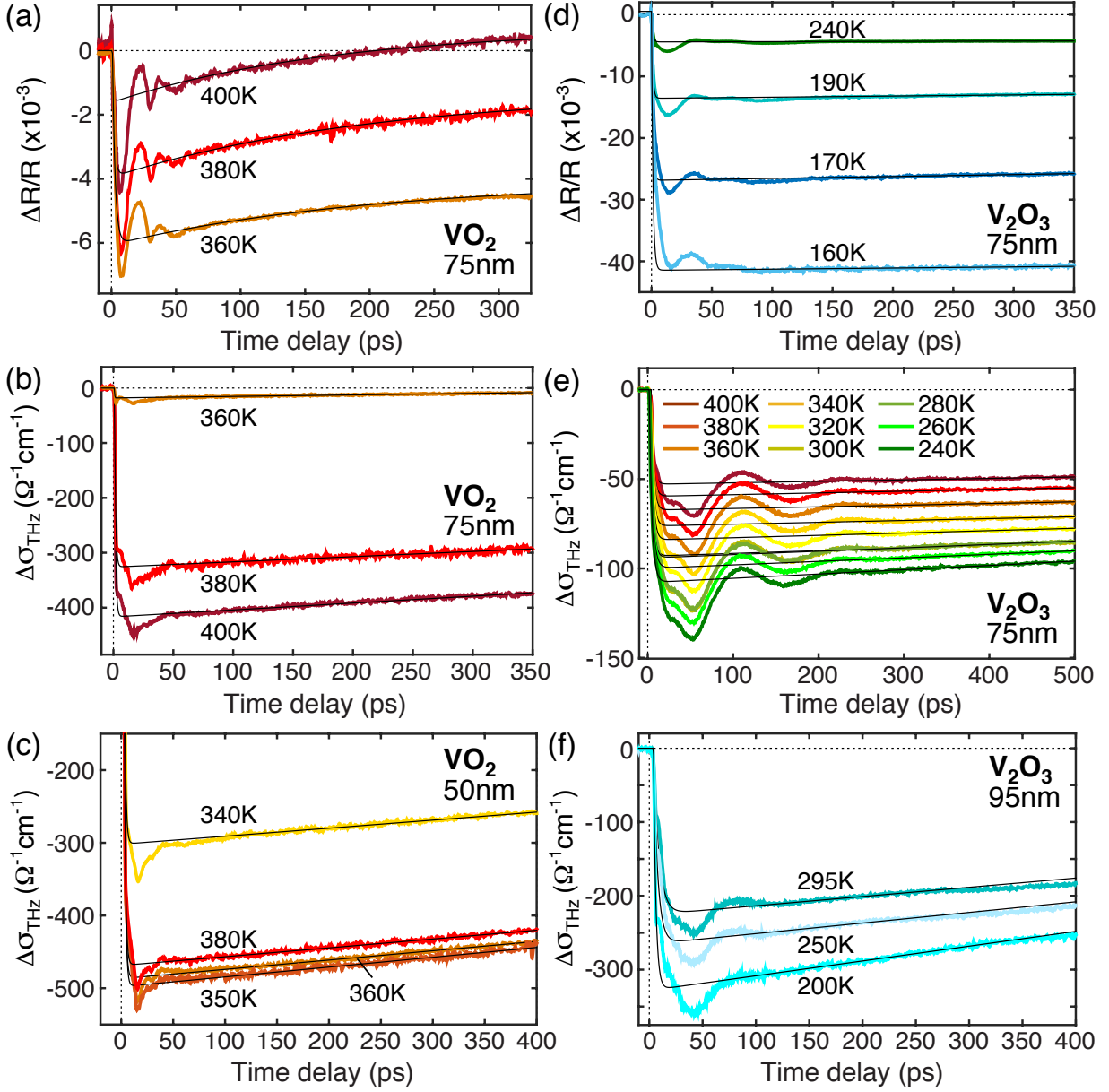


FIG. S4. Full length transient $\Delta R/R$ (a) and $\Delta\sigma$ (b and c) of VO_2 , and $\Delta R/R$ (d) and $\Delta\sigma$ (e and f) of V_2O_3 for temperatures above T_{IMT} . The results correspond to a 75 nm film (a and b) and to a 50 nm film (c), both at a pump fluence of 3.8 mJ/cm^2 . (d) and (e) correspond to a 75 nm film at a pump fluence of 1 mJ/cm^2 , while (f) corresponds to a 95 nm film at a pump fluence of 3 mJ/cm^2 . Superimposed onto the data are black lines corresponding to fits to a sum of exponentials, as detailed in the text.

extract both the oscillation periods (Figs. 5c and 5f) and the damping times (Fig. S5). The chosen fitting function is a damped sinusoid, $R = R_0 + A \times \exp(-t/t_0) \times \sin(2\pi(t - t_c)/\tau)$,

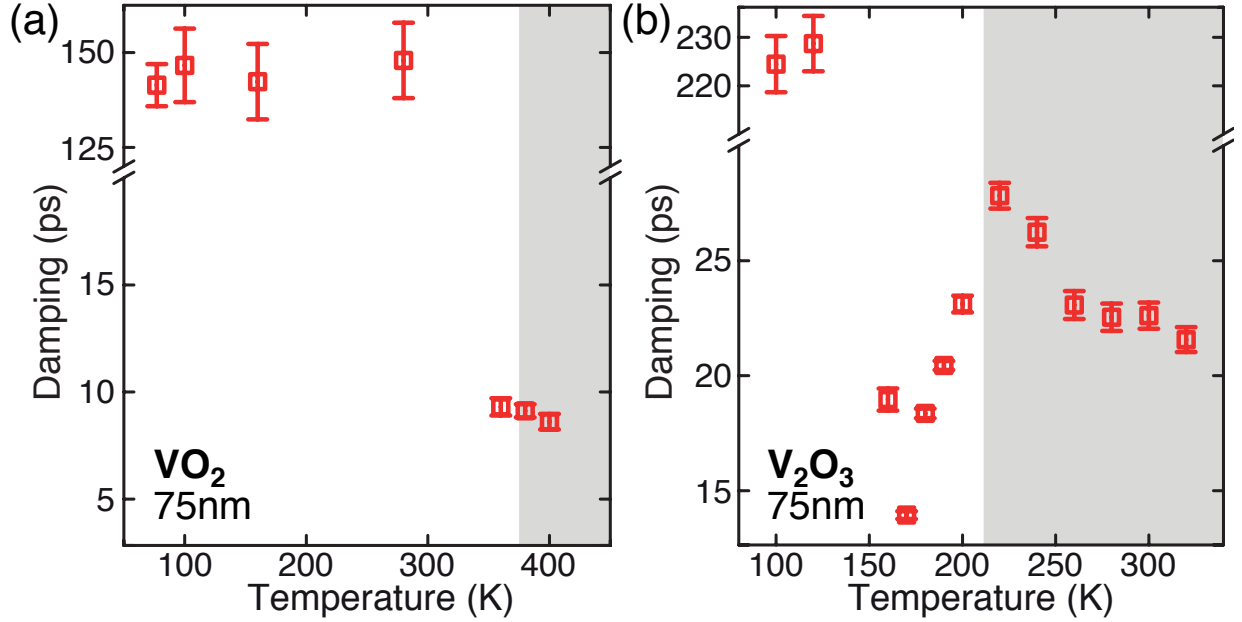


FIG. S5. Damping times extracted from fitting the acoustic component of $\Delta R/R$ dynamics data (shown in Figs. 5a, 5b, 5d and 5e of the main text) to a damped sinusoid. Data are shown for 75 nm thick films of (a) VO₂ and (b) V₂O₃. The fully metallic phase is shaded gray, for comparison with Fig. 1 of the main text.

where τ is the period and t_o is the damping time. Table SII lists the adjusted R² parameters obtained for the fits. These are mostly very close to 1, attesting to the reliability of the damped sinusoid model in describing our data. VO₂ data in the 100 - 160 K range has slightly lower but still very acceptable R² parameters due to a decreased signal-to-noise ratio.

Figure S5 shows the temperature dependent damping times (equivalent to the inverse of the scattering rate) of VO₂ (Fig. S5a) and V₂O₃ (Fig. S5b). Interestingly, we measure a much slower acoustic damping time in the insulating phase of VO₂ compared to the metallic phase (cf. Figs. 5a and 5b of the main text), consistent with the work of Budai *et al.*¹⁷ which shows that phonon-phonon scattering present in the metallic phase essentially disappears in the insulating phase of VO₂. The same temperature dependence of the damping is observed for V₂O₃, with lower values in the metallic phase (Figs. 5d and 5e). An analysis similar to that of Budai *et al.*¹⁷, done on V₂O₃, would provide a measure of the importance of phonon entropy effects in the metallic phase of this material, as compared to VO₂.

It is interesting to note that the damping time for V₂O₃ increases between about 150 K

V_2O_3		VO_2	
T (K)	R^2 (%)	T (K)	R^2 (%)
100	94.8	77	88.4
120	97.5	100	71.7
160	99.1	160	68.9
170	99.8	280	68.3
180	99.8	360	99.5
190	99.9	380	99.7
200	99.7	400	99.1
220	99.7		
240	99.6		
260	99.4		
280	99.3		
300	99.5		
320	99.4		

TABLE SII. Adjusted R^2 parameters obtained for the fits of the acoustic component of $\Delta R/R$ dynamics data with a damped sinusoid, for V_2O_3 (left) and VO_2 (right).

and the start of the shaded region, at 220 K, where full metallic conductivity is reached. Insulating and metallic volume fractions coexist in this 150 - 220 K temperature interval (cf. Fig. 1b in the main text). Insulating regions hinder the propagation of acoustic modulations throughout the metallic volume, thereby decreasing the damping time in the (lower) temperature region where the insulating volume fraction is larger¹⁸. An increasing damping time in the coexistence region could also be a signature of an intermediate monoclinic metallic phase¹⁹⁻²¹. As the system becomes fully metallic (shaded area), and while it remains in the ~ 50 K wide (lower) temperature region where the conductivity is maximal and approximately constant (Fig. 1b), the damping becomes slightly faster as temperature increases — potentially the result of phonon-phonon interactions increasing with temperature. Above 250 K the damping time remains essentially constant until 320 K, the limit of our measurement. A temperature independent damping in the fully metallic phase of V_2O_3 is also consistent with the results of Budai *et al.* on VO_2 ¹⁷, where this effect was

interpreted as a signature of electron-phonon effects contributing to phonon anharmonicity in addition to simply phonon-phonon interactions. Our data also yields a stable damping time for metallic VO₂, over the small temperature interval available from our measurements. The temperature independence of acoustic damping properties in the metallic phase of both materials therefore lends further support to the main message of this manuscript, namely the significance of electron-phonon coupling in VO₂ and V₂O₃.

As shown explicitly in Fig. S5, the acoustic scattering rate is higher in both phases of VO₂ compared to V₂O₃. This can also be seen directly from Figs. 4 and 5 of the main text, where the acoustic modulations persist longer for V₂O₃ than for VO₂. Indeed, the conductivity dynamics (Fig. 4) show that the oscillations essentially disappear 300 ps after photoexcitation for V₂O₃, whereas they have already disappeared around 100 ps in the case of VO₂. Similarly, the reflectivity dynamics (Fig. 5) show a strong decrease in the oscillation amplitude at about 150 ps for V₂O₃, and at about 75 ps for VO₂.

The sensitivity of conductivity and reflectivity dynamics measurements differs but the conclusion is the same - there are fewer decay channels for acoustic excitation in V₂O₃ compared to VO₂. Budai *et al.*¹⁷ have reported that the fast phonon damping in VO₂ arises from a large anharmonicity in the lattice potential. Our present observation suggests a lower degree of anharmonicity for the lattice potential in V₂O₃, compared to VO₂.

E. Low temperature VO₂ and V₂O₃ conductivity dynamics

Figure S6 shows the full time window of the temperature dependent $\Delta\sigma(t)$ for $T < T_{IMT}$, for all four films discussed in the main paper: 75 nm VO₂ (Fig. S6a), 50 nm VO₂ (Fig. S6b), 75 nm V₂O₃ (Fig. S6c) and 95 nm V₂O₃ (Fig. S6d). First, it is clear that for initial temperatures well below T_{IMT} lower initial temperatures lead to lower photoinduced conductivities, regardless of the film thickness or the specific vanadium oxide. For initial temperatures approaching T_{IMT} the film is already partly metallic and the transient conductivity starts to decrease. Second, the onset of the conductivity recovery is clearly seen for the lowest temperatures within the time window, indicating that only a metastable and partially metallic state is achieved. These behaviors are observed in all but Fig. S6c, where the minimum investigated temperature is already quite close to T_{IMT} .

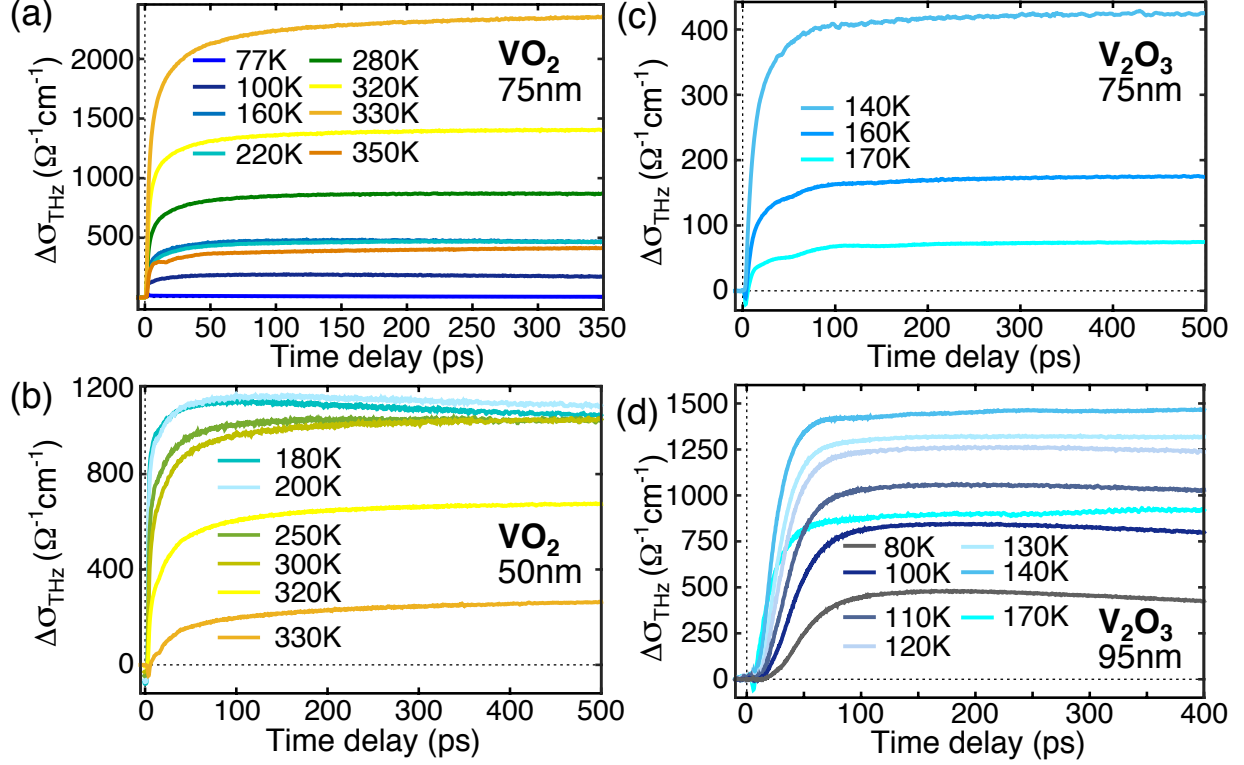


FIG. S6. Conductivity dynamics at $T < T_{IMT}$ for the (a) 75 nm VO_2 , (b) 50 nm VO_2 , (c) 75 nm V_2O_3 , and (d) 95 nm V_2O_3 films. Pump fluences were 3.8 mJ/cm^2 in (a) and (b), 1 mJ/cm^2 in (c), and 3 mJ/cm^2 in (d). The final conductivity as well as the lifetime of the photoexcited metallic state increases with initial temperature. For temperatures close to T_{IMT} the transient conductivity starts to decrease since the film is already partly metallic.

F. Comparison of different film thicknesses

Figure S7 shows the comparison between different film thicknesses for a given material. In Fig. S7a, the acoustic component of $\Delta\sigma(t)$ for the two VO_2 films with different thicknesses of the same orientation and similar characteristics are compared. The acoustic oscillations are clearly faster in the 50 nm film, consistent with a shorter time needed for the acoustic perturbation to cross a thinner film at a comparable sound velocity. The same conclusion can be drawn even more directly from the $\Delta R/R$ dynamics shown in Fig. S7b where a normalized plot comparing the acoustic oscillations for both the 50 nm and 75 nm thicknesses at 360 K is shown. This confirms the validity of our analysis where we relate the oscillation period to the sound velocity in the system.

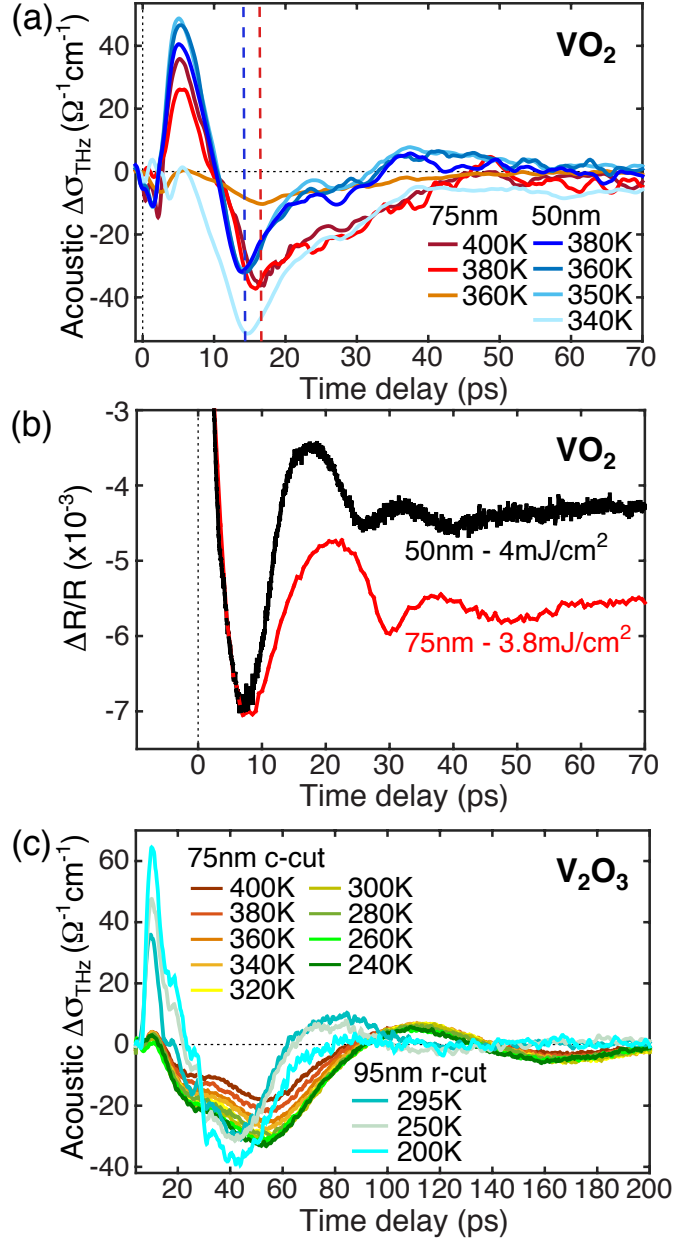


FIG. S7. Comparison for different film thicknesses. Background subtracted $\Delta\sigma$ acoustic oscillations for (a) VO_2 and (c) V_2O_3 , corresponding to the data in (a) Fig. S4b and S4c, and (c) Figs. S4e and S4f. Two film thicknesses are compared for both materials, 75 nm and 50 nm for VO_2 , and 75 nm and 95 nm for V_2O_3 , which exhibit different delays between acoustic oscillations, as discussed in the text. (b) shows $\Delta R/R$ oscillations at 360 K for the same VO_2 films, confirming the shorter delay between oscillations in the thinner film. $\Delta\sigma(t)$ data for both VO_2 films (a) and for the 95 nm V_2O_3 film (c) were smoothed using a five point (1 ps) moving average.

Figure S7c shows the acoustic component of $\Delta\sigma$ for the two V_2O_3 films. In this case it is difficult to compare the oscillation period since the films have different orientations and growth conditions, leading to different properties. In fact, the reflected acoustic signal is faster for the thicker film, contrary to what would be expected and to what is observed in the case of VO_2 . This discrepancy in the V_2O_3 films can be explained by a combination of 1) a different sound propagation direction due to different crystal cuts, 2) different substrate-lattice mismatch in both films, and 3) different degrees of crystallinity. All of these lead to variations in the sound velocity normal to the sample, so that the oscillation period in the two V_2O_3 films cannot be directly compared.

A detailed description beyond the present qualitative discussion of the many additional contributions to the photoinduced acoustic response in such thin films (with thickness on the order of the acoustic wavelength) is outside the scope of the present work.

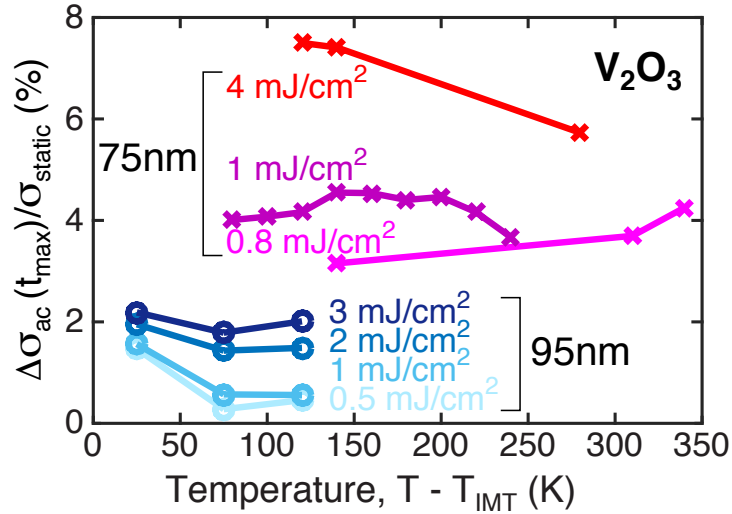


FIG. S8. Fluence dependence of the V_2O_3 conductivity modulation data shown in Fig. 4 of the main text. Data are shown for the 75 nm V_2O_3 film (red/pink) for fluences in the 0.8 - 4 mJ/cm² range, for the 95 nm V_2O_3 film (blue) for fluences in the 0.5 - 3 mJ/cm² range. As expected, the acoustic response increases with photoexcitation fluence.

G. Fluence dependence

Figure S8 depicts the fluence dependence of the V_2O_3 conductivity data shown in Fig. 4 of the main text. As expected, the induced acoustic response increases with fluence. Since

the latent heat of V_2O_3 is significantly lower than that of VO_2 , lower fluences were used for the V_2O_3 measurements at low temperatures. This was maintained for the high temperature measurements, for consistency. Also, the damage threshold for V_2O_3 is five times lower than that for VO_2 ^{3,22}, which limits the fluence values that can be used on V_2O_3 in general. To more effectively compare the observed acoustic modulation of the conductivity between the two materials in Fig. 4 of the main text, 3 mJ/cm² V_2O_3 data on the 95 nm film were chosen, being the closest match to the 3.8 mJ/cm² used for the VO_2 75 nm film. 1 mJ/cm² data were chosen for the 75 nm V_2O_3 film since this is the fluence at which more data points were available for this sample. While it is not possible to deduce a precise functional fluence dependence of the acoustic modulation from this data, the results in Fig. S8 show that the modulation induced in V_2O_3 with a pump fluence of 4 mJ/cm² is about 1.7 times higher than that induced with 1 mJ/cm². Figure 4 in the main text shows that the acoustic modulation in 75 nm thick V_2O_3 following 1 mJ/cm² photoexcitation is larger than that in 75 nm thick VO_2 following 3.8 mJ/cm² photoexcitation. The modulation in 75 nm thick V_2O_3 following 4 mJ/cm² photoexcitation would therefore be even larger. Consequently, the conclusion that the acoustic modulation in V_2O_3 is stronger than that in VO_2 (in the main text, based on Fig. 4) is not affected by the fact that the analysis is done at different fluences.

To be precise in comparing pump induced effects one should consider deposited energy density in the material rather than only incident fluence. In the case of metallic VO_2 and V_2O_3 , however, the penetration depth and reflectivity of the 800 nm wavelength pump beam are very similar, as seen in Table SIII. The slight reduction in absorbed fluence due to a higher reflectivity in VO_2 is compensated by a smaller penetration depth, so that overall fluence values can be directly compared in the metallic phases of the two materials. As a side note, comparing incident fluences at 800 nm is still equivalent to comparing deposited energy densities even in the insulating phase of VO_2 and V_2O_3 (Table SIII).

III. DETAILED ANALYSIS OF A THICKER FILM

We also performed reflectivity measurements on a thicker sample, a 400 nm V_2O_3 film deposited on 70 nm of sapphire with a bulk silicon substrate²⁵, for comparison. Figure S9 shows the corresponding $\Delta R/R$ dynamics at three temperatures above T_{IMT} , for a fluence

	Material	Penetration depth	Reflectivity
Metallic	VO ₂	74 nm	0.19
	V ₂ O ₃	99 nm	0.12
Insulating	VO ₂	82 nm	0.26
	V ₂ O ₃	171 nm	0.13

TABLE III. Penetration depth and reflectivity values for VO₂ and V₂O₃, estimated from dielectric constant measurements^{23,24}.

of 1 mJ/cm². It is clear from this figure that for this larger film thickness, the dynamics are dominated by acoustic echoes of the strain pulse reflecting off the interface. Here a model of the propagating acoustic discontinuity can be attempted, as briefly hinted at in the supporting information of Liu *et al.*³.

In detail, we observe several dynamical stages in Fig. S9. The sub-picosecond peak in (a) is due to electron-electron collisions (ballistic transport) and electronic thermalization. The non-uniform heat absorption across the film generates a coherent strain wave (L₁) which propagates along the film and then reflects from the sample-substrate interface (L₂, at 100 ~ 150 ps). Subsequent acoustic reflections after ~ 150 ps are too small to be detected.

Figure S9b shows a fit of the 220 K $\Delta R/R$ data using the two-temperature model (TTM)²⁶ which tracks the electronic (T_e) and lattice (T_l) temperatures in the first 1.5 ps after excitation,

$$\begin{aligned}
 C_e(T_e) \frac{\partial T_e}{\partial t} &= -g(T_e - T_l) + P(t) \\
 C_l \frac{\partial T_l}{\partial t} &= g(T_e - T_l).
 \end{aligned}$$

Here, the electron specific heat is given by $C_e(T_e) = \gamma T_e$, where $\gamma = 80 \text{ mJ K}^{-2} \text{ mol}^{-1}$, and the lattice specific heat is taken as constant, $C_l = 100 \text{ J K}^{-1} \text{ mol}^{-1}$. $P(t)$ denotes the absorbed pump power density, which accounts for the absorption length of the pump pulse in the sample (cf. discussion of the penetration depth in Section II G, above). These assumptions are valid above T_{IMT} , i.e. when the latent heat contribution is no longer relevant. The only free parameter is the V₂O₃ electron-phonon coupling constant g , for which the TTM fit yields a large value of $g = 3 \times 10^{18} \text{ W K}^{-1} \text{ m}^{-3}$.

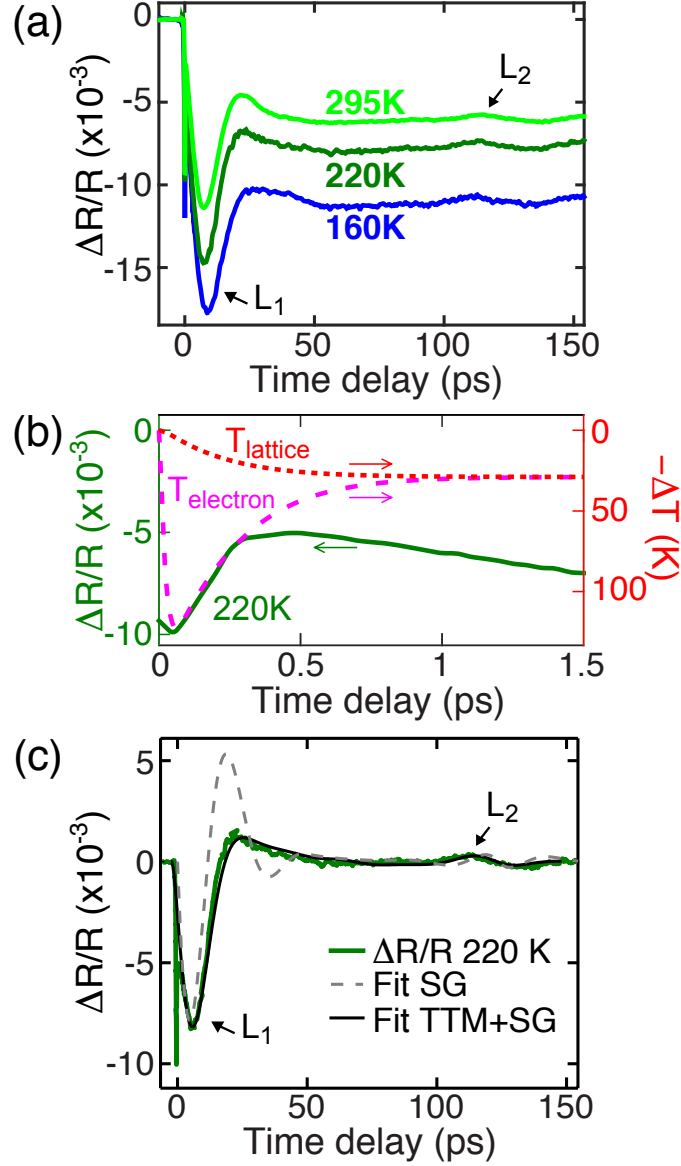


FIG. S9. (a) Reflectivity change $\Delta R/R$ in the 400 nm V_2O_3 film, showing a fast electronic response followed by two acoustic waves signatures, L_1 and L_2 , due to the main acoustic wave and to its reflection from the sample-substrate interface. (b) Two-temperature model fit of the 220 K data (green line, left-hand side y-axis) between 0 and 1.5 ps, yielding an electron-phonon coupling constant of $g = 3 \times 10^{18} \text{ W K}^{-1} \text{ m}^{-3}$. Electronic and lattice temperatures are shown as dashed pink and dotted red lines, respectively, and correspond to the right-hand side y-axis. (c) Fit of the 220 K data (green line) with the strain generation only (SG) model (dashed gray lines) and with the combined two-temperature with strain generation (TTM+SG) model (full black lines).

As shown in Fig. S9b, the TTM successfully fits the electronic response in the initial ~ 0.5 ps, where the electronic temperature constitutes the main contribution to the dynamics of the system. Fitting in this region is sufficient to determine g . The lattice simultaneously heats, as illustrated by the evolution of $T_{lattice}$ in Fig. S9b. Were the response of the lattice purely thermal, as assumed by the TTM, the reflectivity dynamics would track the dynamics of $T_{lattice}$ (and $T_{electron}$). However, some of the energy is transferred to different modes such as the acoustic ones which constitute the focus of this paper. These modulate the spectral weight at 1.55 eV, and consequently the reflectivity dynamics, such that the $\Delta R/R$ diverges from a simple exponentially decaying thermal response, as clearly seen in the larger time window shown in Fig. S9a.

In Figure S9c, the acoustic wave propagation during the first 150 ps is simulated using two different models. The first is a relatively simple strain generation (SG) model^{27,28}, given by

$$\rho \frac{\partial^2 u}{\partial t^2} = 3 \frac{1 - \nu}{1 + \nu} B \frac{\partial^2 u}{\partial z^2} - 3B\beta \frac{\partial \nabla T(z)}{\partial z},$$

where $\rho = 5 \times 10^3$ kg/m³ is the density of the V₂O₃ film, u is the displacement of the lattice normal to the film surface, $\nu = 0.33$ is the Poisson ratio²⁹, $B = 2 \times 10^{11}$ Pa is the bulk modulus of V₂O₃³⁰, z is the acoustic wave propagation direction, $\beta = 2.5 \times 10^{-6}$ is the linear expansion coefficient³¹, and ∇T is the time-independent exponentially decaying temperature gradient across the film, which accounts for the absorption length of the pump pulse.

The displacement $u(z, t)$ obtained from this expression is used to estimate the transient reflectivity amplitude $\Delta R/R$ from

$$\eta = \frac{\partial u}{\partial z}$$

$$\Delta R(t) = \int_0^\infty f(z) \eta(z, t) dz.$$

$f(z)$ is the sensitivity function defined by Thomsen *et al.*²⁸, in which there are two fitting parameters, $\frac{\partial n}{\partial \eta}$ and $\frac{\partial k}{\partial \eta}$. n and k stand for the real and imaginary parts of the refractive index at 800 nm, given by $n = 1.69$ and $k = 0.59$ at 220 K²³. The sound velocity of the

longitudinal strain wave in the film is taken as 8×10^3 m/s^{32,33}. An additional dimensionless fitting parameter is added to account for the attenuation of the acoustic wave upon reflection at the film-substrate interface.

As seen in Fig. S9c (dashed gray lines), this model provides reasonable fits to the data within the first few ps after photoexcitation, but the predicted wave amplitude at about 25 ps is too large to accurately describe the results. The discrepancy in the simulated response is the result of the model not accounting for the non-equilibrium processes at short time delays nor for electron-lattice thermalization in the thin film.

To correct the discrepancy of the first model, Fig. S9c plots also the prediction from a second model, which combines the two-temperature and the strain generation analyses (TTM+SG):

$$\begin{aligned} C_e(T_e) \frac{\partial T_e}{\partial t} &= \nabla(\kappa_e \nabla T_e) - g(T_e - T_l) + P(z, t) \\ C_l \frac{\partial T_l}{\partial t} &= \nabla(\kappa_l \nabla T_l) + g(T_e - T_l) \\ \rho \frac{\partial^2 u}{\partial t^2} &= 3 \frac{1 - \nu}{1 + \nu} B \frac{\partial^2 u}{\partial z^2} - 3B\beta \frac{\partial \nabla T(z, t)}{\partial z}, \end{aligned}$$

where $\kappa_e = 300$ kg m⁻¹ K⁻¹ and $\kappa_l = 30$ kg m⁻¹ K⁻¹ are the thermal conductivities of the electrons and the lattice, respectively.

This model, which accounts for thermalization effects, is significantly more successful in describing our data (dotted gray lines in Fig. S9c), given the choice of $\frac{\partial n}{\partial \eta} = -1.63 \frac{\partial k}{\partial \eta}$, than the individual TTM and SG models.

* elsabreu@phys.ethz.ch. Previously at Department of Physics, Boston University, Boston MA 02215, USA

† Previously at Department of Physics, Boston University, Boston MA 02215, USA

‡ mengkun.liu@stonybrook.edu. Previously at Department of Physics, Boston University, Boston MA 02215, USA

§ raveritt@physics.ucsd.edu. Previously at Department of Physics, Boston University, Boston MA 02215, USA

- ¹ E. Abreu, M. Liu, J. Lu, K. G. West, S. Kittiwatanakul, W. Yin, S. A. Wolf, and R. D. Averitt, *New Journal of Physics* **14**, 083026 (2012).
- ² J. B. Goodenough and H. Y. P. Hong, *Physical Review B* **8**, 1323 (1973).
- ³ M. K. Liu, B. Pardo, J. Zhang, M. M. Qazilbash, S. J. Yun, Z. Fei, J. H. Shin, H.-T. Kim, D. N. Basov, and R. D. Averitt, *Physical Review Letters* **107**, 066403 (2011).
- ⁴ D. B. McWhan, A. Menth, J. P. Remeika, W. F. Brinkman, and T. M. Rice, *Physical Review B* **7**, 1920 (1973).
- ⁵ H. Kuwamoto, J. M. Honig, and J. Appel, *Physical Review B* **22**, 2626 (1980).
- ⁶ M. J. Rozenberg, G. Kotliar, H. Kajueter, G. A. Thomas, D. H. Rapkine, J. M. Honig, and P. Metcalf, *Physical Review Letters* **75**, 105 (2008).
- ⁷ P. Limelette, A. Georges, D. Jérôme, P. Wzietek, P. Metcalf, and J. M. Honig, *Science* **302**, 89 (2003).
- ⁸ F. Rodolakis, P. Hansmann, J. P. Rueff, A. Toschi, M. W. Haverkort, G. Sangiovanni, A. Tanaka, T. Saha-Dasgupta, O. K. Andersen, K. Held, M. Sikora, I. Alliot, J. P. Itié, F. Baudelet, P. Wzietek, P. Metcalf, and M. Marsi, *Physical Review Letters* **104**, 047401 (2010).
- ⁹ D. Kucharczyk and T. Niklewski, *Journal of Applied Crystallography* **12**, 370 (1979).
- ¹⁰ D. B. McWhan and J. P. Remeika, *Physical Review B* **2**, 3734 (1970).
- ¹¹ P. D. Dernier and M. Marezio, *Physical Review B* **2**, 3771 (1970).
- ¹² M. Marezio, D. B. McWhan, J. P. Remeika, and P. D. Dernier, *Physical Review B* **5**, 2541 (1972).
- ¹³ E. Abreu, S. Wang, J. G. Ramírez, M. Liu, J. Zhang, K. Geng, I. K. Schuller, and R. D. Averitt, *Physical Review B* **92**, 085130 (2015).
- ¹⁴ S. Kittiwatanakul, S. A. Wolf, and J. Lu, *Applied Physics Letters* **105**, 073112 (2014).
- ¹⁵ J. Lu, K. G. West, and S. A. Wolf, *Applied Physics Letters* **93**, 262107 (2008).
- ¹⁶ S. Wang, J. G. Ramírez, J. Jeffet, S. Bar-Ad, D. Huppert, and I. K. Schuller, (2016), submitted to *Europhysics Letters*.
- ¹⁷ J. D. Budai, J. Hong, M. E. Manley, E. D. Specht, C. W. Li, J. Z. Tischler, D. L. Abernathy, A. H. Said, B. M. Leu, L. A. Boatner, R. J. McQueeney, and O. Delaire, *Nature* **515**, 535 (2014).
- ¹⁸ J. G. Ramírez, J. De La Venta, S. Wang, T. Saerbeck, A. C. Basaran, X. Batlle, and I. K. Schuller, *Physical Review B* **93**, 214113 (2016).

- ¹⁹ H.-T. Kim, Y. W. Lee, B. J. Kim, B. G. Chae, S. J. Yun, K. Y. Kang, K. J. Han, K. J. Yee, and Y. S. Lim, *Physical Review Letters* **97**, 266401 (2006).
- ²⁰ M. K. Liu, M. Wagner, E. Abreu, S. Kittiwatanakul, A. McLeod, Z. Fei, M. Goldflam, S. Dai, M. M. Fogler, J. Lu, S. A. Wolf, R. D. Averitt, and D. N. Basov, *Physical Review Letters* **111**, 096602 (2013).
- ²¹ H.-T. Kim, M. Kim, A. Sohn, T. Slusar, G. Seo, H. Cheong, and D.-W. Kim, *Journal of Physics: Condensed Matter* **28**, 085602 (2016).
- ²² A. Cavalleri, M. Rini, H. H. W. Chong, S. Fourmaux, T. E. Glover, P. A. Heimann, J. C. Kieffer, and R. W. Schoenlein, *Physical Review Letters* **95**, 2 (2005).
- ²³ M. M. Qazilbash, A. A. Schafgans, K. S. Burch, S. J. Yun, B. G. Chae, B. J. Kim, H.-T. Kim, and D. N. Basov, *Physical Review B* **77**, 115121 (2008).
- ²⁴ H. W. Verleur, A. S. Barker Jr., and C. N. Berglund, *Physical Review* **172**, 788 (1968).
- ²⁵ S. J. Yun, J. W. Lim, J. S. Noh, B. J. Kim, and H. T. Kim, *Japanese Journal of Applied Physics* **48**, 04C139 (2009).
- ²⁶ W. S. Fann, R. Storz, H. W. K. Tom, and J. Bokor, *Physical Review Letters* **68**, 2834 (1992).
- ²⁷ C. Thomsen, J. Strait, Z. Vardeny, H. J. Maris, J. Tauc, and J. J. Hauser, *Physical Review Letters* **53**, 989 (1984).
- ²⁸ C. Thomsen, H. T. Grahn, H. J. Maris, and J. Tauc, *Physical Review B* **34**, 4129 (1986).
- ²⁹ B. S. Allimi, M. Aindow, and S. P. Alpay, *Applied Physics Letters* **93**, 112109 (2008).
- ³⁰ S. R. Hassan, A. Georges, and H. R. Krishnamurthy, *Physical Review Letters* **94**, 036402 (2005).
- ³¹ E. P. Warekois, *Journal of Applied Physics* **31**, 346S (1960).
- ³² W. B. Yelon and J. E. Keem, *Solid State Communications* **29**, 775 (1979).
- ³³ M. M. Seikh, C. Narayana, A. K. Sood, P. Murugavel, M. W. Kim, P. A. Metcalf, J. M. Honig, and C. N. R. Rao, *Solid State Communications* **138**, 466 (2006).

